Determination of Lithium Isotope Concentration by Laser Induced Breakdown Spectroscopy Using Chemometrics

THESIS

Lieutenant Colonel Jason C. Wood, U.S. Army

AFIT/GAP/ENP/18-M20

DEPARTMENT OF THE AIR FORCE
AIR UNIVERSITY

AIR FORCE INSTITUTE OF TECHNOLOGY

Wright-Patterson Air Force Base, Ohio

AFIT/GAP/ENP/18-M20

DETERMINATION OF LITHIUM ISOTOPE CONCENTRATION BY LASER INDUCED BREAKDOWN SPECTROSCOPY USING CHEMOMETRICS

THESIS

Lieutenant Colonel Jason C. Wood, U.S. Army,

Committee Membership:

LTC Michael Shattan
Committee Chair
Assistant Professor, Department of Nuclear Engineer, AFIT

Lt Col Michael Dexter
Member
Assistant Professor, Department of Nuclear Engineering, AFIT

Lt Col Andrew Geyer
Member
Assistant Professor, Department of Mathematics, AFIT

Acknowledgements

Thank you to Ivalee, who bolsters my commitment to a sense of curiosity, and Meridith, who keeps me sane. And humble.

Y'all rock.

Lieutenant Colonel Jason C. Wood, U.S. Army

Abstract

The role of enriched ^{6}Li in nuclear applications makes the ability to detect and monitor lithium enrichment activity imperative. Detecting levels of enrichment of this isotope currently requires sensitive, complex equipment operated by highly-trained technicians, which is prohibitive to rapid detection of enrichment activity. While commercial companies market portable laser induced breakdown spectroscopy (LIBS) with the ability to detect elements on the order or parts per million concentrations, they have not yet been demonstrated to possess the ability to quantitatively determine isotopic concentrations of lithium. This research performs single-pulse LIBS experiments under laboratory conditions to determine concentrations of ^{7}Li and ^{6}Li in solid samples of lithium hydroxide monohydrate in low-pressure argon environments. Spectra containing the atomic emission of lithium near 670.8 nm are collected in LIBS experiments. Chemometric analysis techniques (principal components regression, partial least squares regression, and neural networks analysis) are applied to these collected spectra to develop calibration curves for this equipment. This analysis suggests that bulk lithium isotopic assay can be determined via LIBS *in situ* to within a 95% confidence interval in as little as ten minutes for enrichment levels from 3 to 75%. Evidence of plasma self-absorption in isotopic emission spectra is also measured for the first time. Separately, observation of molecular emissions from LiH and LiO was attempted.

Table of Contents

Page

List of Figures

List of Tables

DETERMINATION OF LITHIUM ISOTOPE CONCENTRATION BY LASER INDUCED BREAKDOWN SPECTROSCOPY USING CHEMOMETRICS

I. Introduction

The purpose of this thesis is to develop a capability to perform LIBS and LAMIS experiments at the Air Force Institute of Technology, and then to inform the design of a field-portable rapid isotopic detection system focused on the detection of lithium isotopes through the application of LIBS and LAMIS. The primary goal of this research was to quantitatively determine the concentration of lithium isotopes in mixed, solid samples of lithium hydroxide monohydrate ($LiOH \cdot H_2O$). This objective was achieved to low accuracy, and it is postulated that additional sampling could improve accuracy to $\pm 1\%$ ^{6}Li fraction in experiments that take less than 15 minutes across the range of isotopic concentration.

This thesis is built in five parts.

Part I is the background and statement of the problem. Here the motivation for this research, the background of the problems associated with isotopic determination of lithium in a field environment, and relevant LIBS strengths and limitations for this application are described.

Part II is theory and literature review. In this part the general theories behind LIBS and its use in current fields of study are reviewed. Chemometric analysis techniques chosen for this research are reviewed and examples of their use in industry today are given.

Part III is the methodology. In this part the experimental setup, the experiment plan, the conditions under which we will conduct experiments and methods by which

we reduce systematic error are described in detail.

Part IV is results. In this part the results of the experiments and analyses are described.

Part V is findings, conclusions and future work. In this part conclusions are drawn from the analyzed data to determine the ability of the experimental set-up to determine isotopic concentrations of lithium in mixed samples. Additionally, future work to further the development of a field-portable, LIBS based detector for determining isotopic concentrations of lithium in a field environment is recommended.

1.1 Background

Lithium is a light, highly-reactive alkali metal that exists on Earth with natural isotopic abundance of 7.59 % ^{6}Li and 92.41% ^{7}Li [1]. Thousands of tons of lithium ore is mined each year by several countries [2]. Of interest to the nuclear community is the use of lithium salts in modern fusion weapons. Here, tritium is generated as part of the fission process through the reactions [3]

$$^{6}Li + n \rightarrow ^{3}H + ^{4}He \tag{1}$$

$$^{7}Li + n \rightarrow ^{3}H + ^{4}He + n^{*} \tag{2}$$

Lithium hydroxide also has several uses in industry, has been used for carbon dioxide capture in the U.S. space program since the Apollo missions [4], and is used in fission reactor control operations [5].

In the last application, ^{6}Li is preferred for its two orders of magnitude larger cross-section for thermal neutron-induced tritium production than ^{7}Li [5, 6]. Such a widely-used and abundant isotope that has such a powerful impact in nuclear weapon development presents a proliferation risk. This risk can be mitigated by monitoring

lithium enrichment facilities in nations that have not yet demonstrated fusion weapon capability, and nations that have not yet demonstrated fission nuclear weapons capability, but have access to special nuclear material.

1.2 Isotopic Determination in the Field - Current Methods

Measurement of stable isotope abundance in a sample by any method is exceptionally difficult. Differentiating the concentrations of atoms and molecules that are separated in mass by the weight of one atomic mass unit requires precision of a very high order. Current methods for isotopic detection use sensitive equipment in laboratory environments. Very few examples of field measurement of stable isotopes exist in literature. One group from LANL did show a limited capability previously by using a backpack LIBS device to detect the isotopic shift of lithium in samples of 92.5% ^{7}LiCl and 95% ^{6}LiCl [7]. This yielded only a qualitative ability measure the enrichment difference between samples.

A typical example of lithium isotope determination can be seen in geological studies. Used as an indicator of water-rock interaction, the French Geological Survey (BRGM) reported the use of laser ablation inductively coupled plasma mass spectrometry (LA-ICP-MS) as a new method for lithium isotope measurement [8]. This technique is performed in a laboratory and shows little, if any, promise for field application.

Smith *et. al.* first reported on the use of LIBS for actinide isotopic measurement in 2000 [9, 10] with Miyabe *et. al.* completing additional work in this area much more recently [11]. However, there is little value to the nuclear community of LIBS for actinide measurement as unstable actinide concentrations can also be measured with gamma spectroscopy. This is not the case for the stable lithium isotopes.

Real-time field measurements of stable isotopes in water and CO_2 by Fourier

transform infrared (FTIR) spectrometry were found to allow periodic sampling of ^{12}C / ^{13}C ratios over a 3-week period [12]. While this field-portable solution could be used to measure lithium isotope concentrations, FTIR requires a sample to be in the gas phase as FTIR requires light to be passed through the sample for the absorbance spectrum to be measured. Because of this necessity, measurements of lithium salts would require sample preparation. While this could be possible, it may not be convenient, and LIBS offers a technique requiring no sample preparation.

In another experiment, it was shown that quantum cascade laser absorption spectroscopy (QCLAS) was superior to existing methods in identifying the isotopologues of N_2O formed in soil decomposition [13]. This study measured absorption in gas samples taken from variously prepared soils. Again, as an absorption-driven method, this technique would require sample preparation (vaporization) in lithium salts. Finally, the study discusses the potential of the future ability of robust systems that allow for field use, whereas LIBS devices are already commercially available and proven.

1.3 Contemporary Proliferation Environment

Isotopic determination in field environments could be of interest for the operations of several organizations worldwide and lithium isotope measurement in the field has clear applications in defense, intelligence and policy mission spaces. Within the Department of Defense, the addition of this capability within the 20th Chemical, Biological, Radiological, Nuclear and Explosives Command and Weapons of Mass Destruction Civil Support Teams could support nuclear consequence management and post-blast analysis missions [14]. The ability to chemically determine the presence of enriched lithium quickly could serve to rapidly narrow the list of suspect actors following an attack, as well as inform Federal Emergency Management Agency (FEMA) response actions. It would not be surprising if many foreign nations could make use

of this capability as well.

Internationally, the International Atomic Energy Agency (IAEA) could benefit from this capability as lithium is widely used in a number of non-nuclear commercial applications as highlighted above. Its presence in national and commercial laboratories with an expressed need presents little concern, and the chemical purification of lithium might also appear benign.

Such nations that could present a need for monitoring include those with a supply of lithium, the industrial knowledge and capability to perform the column exchange (COLEX) enrichment process, and produce lithium-bearing commercial materials where depleted lithium may be used without suspicion. In this process [5], the natural chemical affinity of ^{6}Li for mercury is exploited. As COLEX is not used in other chemical enrichment processes, its presence is suggestive of lithium enrichment. Pakistan, Iran and North Korea all possess the industrial capability to effectively perform such processes and are nations that are openly attempting to advance their nuclear capability.

Inspections of lithium enrichment (i.e. isotope separation) facilities, could be conducted legally under the IAEA Safeguards outlined in the Nonproliferation Treaty (NPT) standard agreement. The difficultly would be to identify and receive approval to inspect facilities not already named as nuclear-technology related facilities. The Institute for Science and International Security (ISIS) reported in 2016 that North Korea was already operating a lithium enrichment facility [15], and their 2017 claim of detonating a fusion weapon would suggest they already possess enriched lithium in quantities sufficient to create fusion weapons.

1.4 LIBS in Nuclear Engineering Applications

LIBS has many applications in nuclear engineering applications to include detection of oxides and fluorides of fissionable material (such as UF_6 in piping), fission products and special nuclear material alloys [16, 17, 18]. Martin *et. al.* achieved limits of detection on strontium, cesium and cerium of 10, 600, and 100 ppm, respectively [17]. Another example is Shattan *et. al.*, who reported limits of detection of 250 ppm in uranyl fluoride detection [18].

1.5 Chemometrics in Spectroscopic Analysis

Chemometrics is a branch of statistics that correlates quality parameters or physical properties to analytical instrument data [19]. Common techniques applied in chemometric analysis include principal components analysis (PCA), partial least squares regression (PLS) and artificial neural networks (ANN).

Recently, chemometric techniques have been applied to spectral data to quantitatively determine chemical properties of the experimental unit. One such example is a case study of 200 different Chinese topsoils where LIBS spectra were analyzed using chemometrics to create calibration curves for eight chemical properties to include pH and chemical concentrations of phosphorous and nitrogen [20]. This effort included a comparison of spectral features in the dataset used for analysis, where the differences between using the full spectra and the spectra of select peaks were found to yield similar results [20]. In a similar study where chromium concentration was targeted for measurement, ANN was shown to be superior to PLS in the analysis of LIBS spectra [21].

Chemometrics is available in nominally any data science-oriented programming language. While PCA and PLS are relatively straight-forward to perform with data science languages, neural networks can create some difficulty in programming due

to their complexity and very large number of parameters. Extensive open-source libraries have been developed by machine learning organizations (Google included with its TensorFlow library) and interested individuals that make ANN and deep neural networks (DNN) accessible to reasonably powered computers. Because of this, algorithms can be easily produced for handheld devices that are accessible to users.

II. Theory and Literature Review

2.1 Laser Induced Breakdown Spectroscopy (LIBS)

LIBS is an optical emission spectroscopy method that uses a focused, pulsed laser to generate a microplasma of ablated material, and a gated spectrometer to capture the optical emission of that microplasma within a certain time range after formation. The de-excitation of ions, atoms and molecules releases photons characteristic of that transition. To appropriately analyze and understand the spectrum from a LIBS experiment, some knowledge of plasma dynamics is necessary.

LIBS has been used for nearly two decades to perform analytical chemistry and elemental identification [22, 7, 23, 24, 18]. Commercial handheld and backpack LIBS systems [18, 7] are available and used to qualitatively determine elemental composition, and have been demonstrated to be able to detect lithium isotopes, if only in an enriched form [7].

Pulsed lasers with nanosecond pulse widths are commonly used in LIBS, and more recently picosecond and femtosecond length pulses have been used [25, 26, 27]. The shorter femtosecond pulse width allows for faster energy deposition, which produces the plasma plume through Coulombic interaction vice thermal expansion, which reduces plasma shielding of the laser pulse [28].

2.2 Time Evolution of Plasma Emission

This microplasma, composed of free electrons, ions and neutral atoms produces powerful, local electric fields. Using nanosecond lasers, laser-induced plasmas (LIP) are produced using pulsed lasers of tens of millijoules pulse energy that are focused on the sample. Taken nearly verbatim from Cremers Handbook of LIBS, irradiance on the order of 10^{10} W/cm^2 typically produce plasmas with temperatures from 8,000

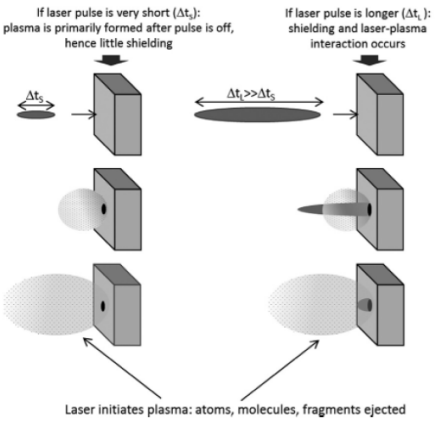

Figure 1. The effect of laser pulse length on the laser–material interaction. Here the shorter laser pulse length is shown to allow laser interaction with the surface of the sample absent any ablated material that would attenuate the laser signal [28].

- 10,000 K 1-2 μs after formation [28]. These achieve ionization levels near 10% for single laser ablation (SP-LIBS), and higher with double laser ablation (DP-LIBS), which uses a second laser pulse to re-excite plasma constituents formed by the first laser pulse [28]. A spectrometer collects and diffracts the emission and a gated, intensified charge-coupled device (ICCD) captures the image (see Figure 2). It is

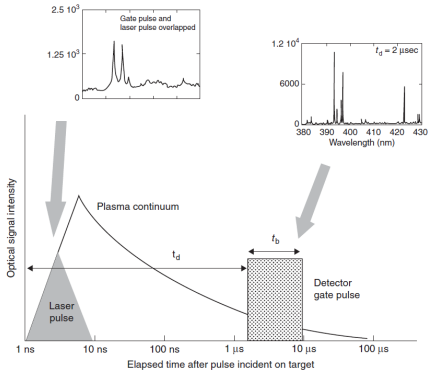

Figure 2. A schematic overview of the temporal history of a LIBS plasma. The gate delay and window are shown. Inserts illustrate the kind of spectra one might observe at the different times [28].

important to note that the temperatures achieved in the plasma is largely dependent on the laser irradiance. Irradiance is a measure of power per unit area, and so increases with shorter pulse duration. Additionally, shorter pulse lengths allow all of the laser

pulse to interact with the material prior to plasma formation. In the case of a longer (ns) pulse, the tail of the pulse will interact with the plasma, and not the sample, during formation. In this way, LIBS using shorter laser pulses allows for more coupling of the laser and target, as well as higher irradiance for a given pulse energy.

As shown in figure 2, spectra from early plasma evolution times show greater intensity and broader peaks than do those taken at later time. At the point of greatest plasma energy, electron temperatures of 10,000 to 15,000 K, and electron densities on the order of 10^{15} to 10^{18} cm^{-3} are achieved [28]. At these temperatures, atomic emissions are broadened by a Doppler effect. They have sufficient kinetic energy to shift the spectrum of light they emit, and effectively red shift and blue shift light emitted as they travel toward and away from the detector, respectively.

Additionally, ions and free electrons produce strong, local electric fields that can shift spectral peaks (Stark shift), as well as broaden spectral lines (Stark broadening) [28]. Magnetic fields are generally not strong enough to shift lines in plasmas of this temperature and ionization state when atomic emission is dominant, and magnetic (Zeeman) broadening is not pronounced [28].

Early in a plasma's lifetime, when it is hottest, its spectrum is dominated by continuum radiation (bremsstrahlung). This emission offers no information about chemical constituents as the plasma emits similar to a blackbody. For this reason LIBS uses observations of the plasma emission at 1-5 μs after formation when continuum radiation is much weaker.

2.3 Matrix Effects

Physical matrix effects are those introduced by the physical structure of the sample, such as varying density and heterogeneous chemical distribution. Heterogeneity of a material can be introduced by grain size of constituent material (e.g. topsoil vs.

milled flour) and is an important factor to understand the plasma formed following ablation. To understand a sample's average composition, the sample heterogeneity must also be understood.

Conversely, the small laser spot size resulting from focusing the laser on the sample allows spatial sampling with some fidelity, and two dimensional mapping of a sample's surface is common [29]. Three dimensional mapping, where depth is probed as well, is also possible [30]. In three dimensional mapping, any density changes will alter the volume of material, and thus depth of material ablated in each laser-sample interaction and the emission spectra will be nominally less intense in less dense material [31].

Reducing the physical matrix effect by milling the powder to a grain size smaller than the focused laser spot can "make LIBS very sensitive to any inhomogeneity of the specimen" [31]. This research takes advantage of milling powders since it involves introducing inhomogeneity in the sample. By deeming one isotope to be a known contaminant, we are in effect measuring the purity, or contamination, in each sample.

Chemical matrix effects are those introduced by the chemical nature of the sample. These can be caused by ionization energies and absorption cross-sections at the laser wavelength which can lead to one element being preferentially excited and ionized over others in the sample. Another source of matrix effect are elements in the sample that interfere with the desired spectral lines.

Easily ionized elements, such as cesium, rob energy from the rest of the system, and can significantly change the intensity of spectral lines produced in the plasma emission [28]. This reduction in the intensity of a spectral line can affect quantitative calculations. Also, elements with high intensity emissions such as sodium, potassium and calcium, or those producing a rich spectra of densely packed lines such as iron, can obscure emissions in nearby wavelengths, making comparative intensity calculations very difficult.

Chemical matrix effects can be partly mitigated during post-processing, or by the application of statistical approaches such as chemometrics [28]. Interferent peaks can be removed in post-processing in any number of ways to include reducing the spectra to some bandwidth [20]. For example, the Li I peaks at 670.776 and 670.791 nm are surrounded by Fe I and Fe II peaks at 670.743 and 670.888 nm, so this interference may be removed by fitting the peaks and removing them from the spectra in post-processing. Also, heterogeneous distribution of impurities can be "averaged out" if many spectra of a sample are taken [7]. In this last approach, one must be mindful of sample heterogeneity to ensure that the sample is homogeneous within the conditions of spectra collection (i.e. to ensure only the contaminant is varying with spatial changes).

2.4 Self-Absorption

Self-absorption is a well-known phenomenon that occurs in plasma. This phenomenon occurs when emission from atoms at the hotter interior of a plasma are absorbed by atoms of the same element in the cooler exterior of the plasma [28]. This manifests as peak cropping or self-reversal of a spectral peak created by the narrow absorption bandwidth of a specific transition [28, 32, 33, 34]. Peak cropping or self-reversal occurs because emission spectra are broadened by thermal and electromagnetic effects, but absorption spectra remains characteristic of the transition energy, so only a very specific energy is absorbed by other atoms or ions. This effect removes just a narrow bandwidth from the spectral emission, which produces the cropped peak, or self-reversal in strong cases.

Both theoretical and experimental methods for correcting for self-absorption have been applied to LIBS measurements. Theoretical corrections include modeling an optically thick plasma to produce a "curve of growth" approach whereby total self-

absorption is found to be proportional to the emission line intensity [34]. The curve of growth is defined to be the logarithmic relationship between the self-absorption coefficient (the fraction of emission intensity attenuated by self-absorption) and the product of the lower energy state emitter population, oscillator strength and path length of the characteristic photon [34, 32]. Experimentally, corrections can be made by comparing sample measurements with and without a mirror behind the plasma, where a coefficient of absorption can be determined [32]. This has been shown to significantly improve the accuracy of calibration curves [33, 35].

2.5 LIBS for Isotopic Determination - Challenges

The difficulty of measuring concentrations of a sample containing two isotopes with LIBS is that the spectral shift in atomic emission can be exceptionally small. Using a portable (backpack) LIBS device, Cremers *et. al.* measured this shift in lithium to be on the order of fifteen picometers [7]. From this measurement it is clear that measuring relative quantities of isotopes in mixed samples would require additional experimental steps to discriminate these spectra.

Spectral broadening presents a significant challenge to LIBS for quantitative isotopic analysis. In his LIBS Handbook, Cremers calculated Stark broadening of commonly analyzed lines in typical LIBS plasmas of 10,000 K and electron densities of $10^{17} cm^{-3}$ [28]. In lithium, this broadening ranges from 8 nm at 413.2 nm to just 28 pm near 670.7 nm whereas Doppler broadening is shown to be on the order of picometers for atomic spectra [28], and is detrimental to using LIBS for quantitative isotopic determination since the isotopic shift in atomic spectra can be on the same order as the Stark width. Cremers reported that this effect prevented resolution of the signature peaks of lithium isotopes [7].

2.6 LIBS for Isotopic Determination - Potential Solutions

Improving system resolution is one method to improve LIBS results, but necessitates a large, sensitive, expensive spectrometer that would not be portable. In this research spectral resolution was achieved by using one spectrometer with a relatively long path length. Another measure was to improve the signal to noise ratio of the signal, thus improving resolution. This increase in signal to noise ratio allowed for later gate delays, which reduces broadening.

One example of an attempt to improve resolution and SNR would be Cremers' 2011 investigation. In his work, Cremers *et. al.* [7] used LIBS in the investigation of lithium isotopes. Here, prepared samples of varying concentrations of LiCl (99%, 92.5% ^{7}Li, ^{6}Li) and Li_2CO_3 (greater than 99%, enriched to 96% ^{6}Li) were interrogated with a portable (backpack) LIBS probe in open atmosphere. Two high-resolution spectrometers gathered the generated spectrum. The DEMON (LTB Berlin) provided a very high resolving power ($\Delta\lambda/\lambda \approx 75{,}000$) over a narrow simultaneous spectral coverage (up to 10 nm from a given wavelength), and a EMU-65 (Catalina Scientific Instruments) with less resolving power ($\Delta\lambda/\lambda \approx 44{,}000$) over a wider simultaneous spectral coverage (190-1100 nm).

2.7 Laser Ablation Molecular Isotopic Spectrometry (LAMIS)

LAMIS is an optical emission spectroscopy technique introduced by Russo *et. al.* [36] in 2011 to determine isotopic content in laser produced plasmas (LPP). LAMIS takes advantage of the changes in molecular rovibrational energy states created by mass changes that are typically larger than those present in atomic emission spectra. Specifically, the mass difference between light isotopes will create larger changes in molecular emission spectra than occur in atomic emission spectra [36]. The same phenomenon is present in the molecular emissions of heavy isotopes, but the effect is less

pronounced. In this way LAMIS provides advantages over LIBS for isotopic determination because the isotopic shifts are potentially larger than the LPP broadening effects (nanometers versus tens of picometers).

LAMIS observes the plasma using a gate delay larger than that normally seen in LIBS (50+ μs versus 1-5 μs) to allow atoms to combine and form diatomic molecules so that molecular spectra can be observed. This is beneficial due to the relative simplicity of modeling diatomic molecules, early formation and their large abundance in cooling plasmas. However, as the gate delay increases, the intensity of the emission decreases and a compromise between intensity and signal-to-noise ratio must be made. As diatomic molecules are among the first molecules formed, they should form when the temperature is high enough to produce excitation, and thus molecular emission upon de-excitation.

The National Institute of Standards and Technology (NIST) maintains a database of elemental spectral lines, many of which are deeply studied, and experiment results for some diatomic molecular spectra are also catalogued. Further, modeling software such as PGOPHER [37] and LEVEL [38] can be used to predict spectra produced in rovibrational state transitions. These models can help determine like molecular emissions that can be observed and compared in experiment.

The advantages of LAMIS are stark when comparing the difference in the isotopic shift in spectra collected from LIBS experiments on ^{10}B and ^{11}B and ^{10}BO and ^{11}BO [36]. In the atomic spectrum the isotopic shift is shown to be 0.002 nm, and the molecular shift is 0.73 nm [36]. This two order of magnitude shift is more easily distinguished by lower resolution spectrometers and is expected to be much larger than the effects of Doppler and Stark Broadening. In the molecular spectra of OH and OD produced from plasma emission from ablating vapors in open atmosphere at a gate delay of 60 μs and a gate width of 25 μs [36, 39], the shift was measured

to be 0.68 nm, which exceeds the 0.18 nm atomic line, and is less prone to Stark broadening [36]. Finally, observation of the ^{12}C and ^{13}C emissions in coal samples and the molecular emission spectra of CN and C_2 [36, 40] showed a separation up to 0.30 nm [36].

In a study of matrix effects in LAMIS, Brown *et. al.* highlights pitfalls associated with experiment in the presence of additional elements present in field samples [41]. In this case molecular emissions of BO and BN in the 255-265 nm region were measured [41]. This region was selected to mimic performance in the field as a nuclear forensics and national security applications, where sunlight would interfere least with deep UV emissions [41]. Matrix effects were observed due to surface roughness effects on laser focus, and more highly mixed sample formed isotopologues that affected performance of least-squares fitting [41].

In another study, DP-LAMIS was performed to compare detection limits achievable by SP-LAMIS using a 10.6 μm laser to apply the second pulse [42]. Here, samples of H_3BO_3 were ablated and their limits of detection evaluated. The results showed that the additional laser increased the plasma temperature up to twice that of LIBS, with a slightly better limit of detection (2.3-2.4%) than previously reported [36, 41].

2.8 LAMIS Challenges in Isotopic Determination and Potential Solutions

LAMIS challenges to isotopic determination include the much weaker intensity of molecular emissions, matrix effects (as in LIBS) and the complexity of those emissions.

Weak spectral emissions observed at the late time of molecular emission are due to the lower population of molecules formed from the plasma by comparison to atoms and the lower transition intensities of molecular states. SNR improvement techniques can help to mitigate this issue. For example, double-pulse LAMIS (DP-LAMIS) is expected to help as DP-LIBS has been demonstrated to increase emission up to 300

times using optimized inter-pulse delay and laser energies [43].

Molecular emissions are also difficult to both model and identify owing to the number of combinations of atomic, vibrational and rotational transitions possible [44]. However, the emissions of LiH are well modeled, likely due to its simple molecular structure. Skenderovic *et. al.* show this spectra to be very rich and contain many overlapping spectral peaks [45]. Because of this, emission from molecular transitions manifest as spectral bands, and not spectral lines, as is apparent in the also well-studied Swan bands of C_2 (see figure 3).

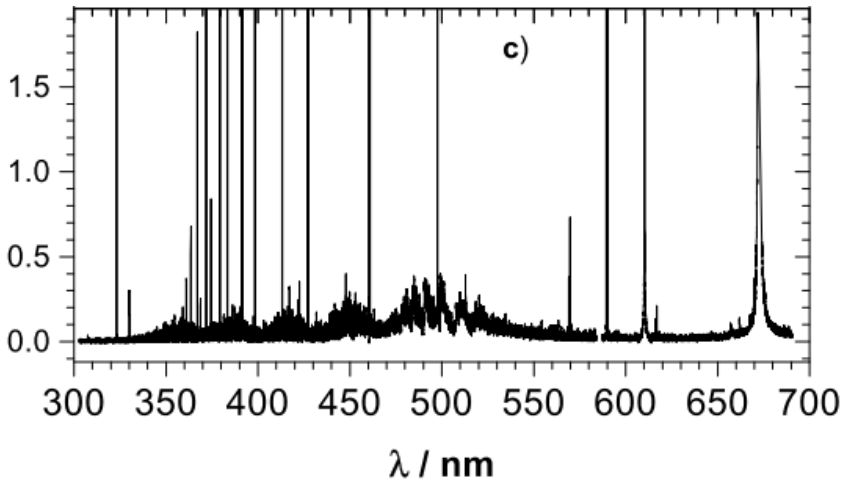

Figure 3. Emission spectrum from the Li and H_2 discharge in a heat-pipe oven. Two molecular features emerge in the regions of 460–550 nm, and 330–470 nm.

Weidman *et. al.* showed the difficulty of observing molecular spectra in samples contining low concentrations (7 $\mu g/cm^2$) of 2,4,6 trinitrotoluene, and they were unable to detect the molecular C_2 bond using DP-LIBS [46]. This result was attributed to several factors, to include the low density of TNT residue in the plasma, the weakness of the oscillator of that bond by comparison to the CN strength, and the chemistry of TNT that would make C_2 unlikely to form in the presence of NO_2 groups [46].

2.9 Lithium.

Lithium contains three protons and three electrons with naturally occurring isotopes containing either 3 or 4 neutrons. It is located below hydrogen in Group 1 on the periodic table indicating its outermost electron is in an s-orbital, and its ground state electron configuration is $1s^2 2s$ with 440 energy levels, 182 of which are found Li I (non-ionized lithium) [47]. It is highly reactive in its elementally pure form, so much so that it sustains burning in standard atmosphere once heated, and exists primarily in nature as a salt.

The neutral lithium emission spectra's strongest and second strongest lines are at 670.7926 nm and 670.7775 nm, respectively. These are produced from the $1s^2 2p$ to $1s^2 2s$ transition with a difference caused by differing total angular momentum (**J**=3/2, 1/2 respectively, see table 1) [48] .

Configuration	Term	J	Level(eV)
2s	2S	1/2	0.000
2p	2P°	1/2	1.847810
		3/2	1.847852
3s	2S	1/2	3.373116
3p	2P°	1/2	3.834269
		3/2	3.834281
3d	2D	3/2	3.878593
		5/2	3.878598
4p	2P°	1/2	4.521661
		3/2	4.521665
4d	2D	3/2	4.540702
		5/2	4.540704
Li II 1s2 (1S0)	Limit		5.391754

Table 1. Li I energy levels [48].

2.9.1 Lithium Species of Interest for LIBS.

For LIBS, the emitting species of interest are neutral (Li I) and singly-ionized (Li II) lithium. While doubly (Li III) and fully-ionized lithium (Li IV) atoms may exist

within the plasma, their population should be much smaller than Li I and Li II at the temperature in LPPs used for LIBS analysis.

The first, second and third ionization energies of lithium are 5.39, 75.64 and 122.45 eV respectively [49]. Therefore, any lithium-containing plasma emitting with a temperature below 5.39 eV ($\approx$ 62,500 K) is below the temperature needed to significantly ionize lithium. Further, the 20,000 K ($\approx$ 1.72 eV) temperatures expected from plasmas in this experiment suggest Li I will be dominant.

For this experiment, observations were made between 660 and 680 nm, where the well-documented line of Li I is near 670.8 nm and Li II lines show near 664, 666, 668 and 678 nm [49].

2.9.2 Chemical Species of Interest for LAMIS.

For LAMIS, the emitting species of interest is lithium hydride (LiH) and lithium monoxide (LiO). To better understand where transitions could be observed, the LEVEL [38] software package was used to simulate molecular emissions from transitions in the the first vibrational state of the molecule. In glow discharge tubes, the $A^1\Sigma^+ \rightarrow X^1\Sigma^+$ transition band head has been observed in LiH near the 330–470 nm range, as well as in the 385 nm area [45]. LiO emission has been observed in a large spectral region between 450 and 570 nm [50]. These wide molecular bands make high resolution spectroscopy difficult as the spectrum observed by such devices is perhaps 30 nm. To detect a molecular band 120 nm wide is thus very challenging.

2.10 Chemometrics

Chemometrics is useful where many replications of an experiment are available for analysis. These replicates can then be used to build a statistical model from mathematically decomposed data, or the data itself. LIBS and LAMIS fit these

requirements since experiments are conducted at the speed of the laser repetition rate, often on the order of 10 Hz or faster. Large data sets are relatively easy to collect when sample sizes allow many experiments to be performed.

As with all statistical models, there is a danger of overfitting and underfitting (too many, too few variables respectively) [51]. To detect such problems cross-validation of the model chosen (specifically the number of variables considered) is performed. This technique is essentially the splitting of data into a training set from which to build a model, and a test set on which to test a model's performance.

Three chemometrics techniques performed with some frequency are principal components analysis (PCA), partial least squares regression (PLS) and neural networks analysis (NNA). In this document, NNA is also referred to as artificial neural networks (ANN) or deep neural networks (DNN). These latter two refer to a statistical model and not a general category within machine learning (i.e. to perform NNA you build an ANN or DNN).

2.10.1 Principal Component Regression (PCR).

Principal Components Analysis (PCA) is an unsupervised decomposition and projection method, more specifically, a dimension-reduction method that chooses the fewest variables to describe the most variance within data given that variables are linear combinations (principal components or PCs) of data sets [51, 52]. Unsupervised decomposition techniques are those that do not take into account the variance of the response vector. PCA is performed through the decomposition of a data matrix $X_{M\times N}$ with N features and M replicates by equation 3.

$$X = T_{M\times F}P^{T}_{N\times F} + E \tag{3}$$

where F is the number of principal components.

Here, P is the collection of N principal components each with F dimensions, or loadings matrix, and T the projection matrix of the data onto the principal component space, or scores matrix [51]. Scores help to visualize the variance explained

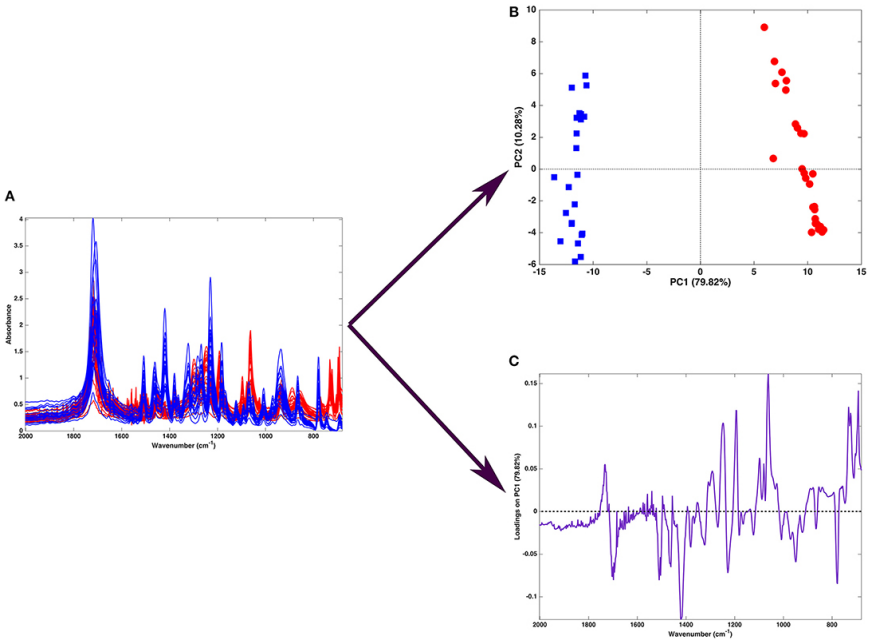

Figure 4. Application of PCA on absorption spectral data taken during drug quality control testing. (A) 51 spectra recorded on samples containing two chemicals. (B) Scores plot showing two clusters corresponding to the tablet makeup separated along the first PC. (C) Loadings plot showing how much PC1 contributes to data variance [51].

by each PC where loadings predict where data will occur along a PC (positive loadings suggest best intensity along the PC in the positive region, and vice versa) [51]. For the example in figure 4, one would expect better absorption of radiation with wavenumbers having negative loadings on PC1 by the chemical indicated with blue squares since it has negative values along PC1 [51, 52].

Principal component regression (PCR) performs least squares fitting to PCs in order to develop a calibration curve that will approximate the response given a selected number of PCs. In this way, measured spectra can be matched to predicted results to develop confidence in a prediction.

PCA has been used effectively to categorize samples using LIBS and similar spec-

troscopic data among others. Applications include counterfeit detection, quality control and soil monitoring [53, 54, 55, 56, 57].

2.10.2 Partial Least Squares Regression (PLS).

PLS is akin to PCR with the exception that PLS is a supervised decomposition method, and the model maximizes the covariance in the response as well as in the PCs [51]. Here the data matrix $X_{M\times N}$ with N features and M replicates is decomposed by equation 4.

$$T = XR \tag{4}$$

where T is the matrix of orthogonal vectors such that X is projected on the direction of maximum covariance with the response, and R is the corresponding matrix of weights onto which the data should be projected [51]. This predicted response is then regressed onto the known response.

PLS has also been used to categorize samples using LIBS and other spectroscopy techniques, usually for quantitative analysis [58, 56, 57]. In this regard it has been shown to perform better than PCA [57, 56] and Martin *et. al.* achieved RMSE values of 0.25% [56]. Also, Zhang *et. al.* showed PLS to be as a viable candidate for correcting spectral interferences where one chemical spectra interferes with the observation of another [58].

For light isotopes, Bolshakov *et. al.* used chemometrics techniques to determine the isotopic ratio to a standard deviation of 0.45% and a sensitivity of 1% or less with no need for very high spectral resolution [39]. Russo *et. al.* performed chemometrics with similar systems used in other work [36], using a gate delay of 10 μs and a gate width of 100 μs to measure the molecular lines of AlO (see figure 5 as well as CaCl to determine the shift in isotopes of Al and Ca, respectively [39].

Partial least squares regression (PLS) applied to LAMIS spectra has been shown

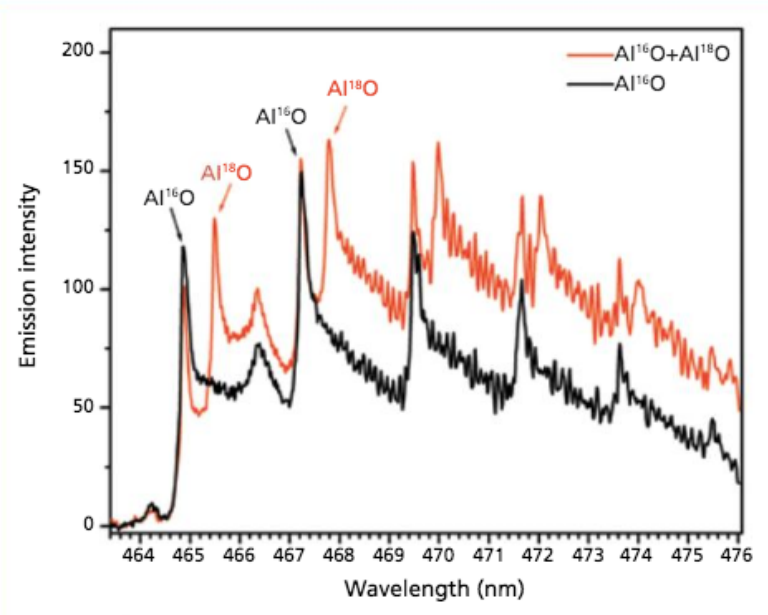

Figure 5. Emission spectra of AlO vibrational band progression (B→X; $\Delta\nu = +1$) formed during ablation of Al_2O_3 natural and ^{18}O-enriched pellets. Spectra were acquired with a 20-μs delay and averaged over 100 laser pulses [39]. Here the isotopic shift is observed to be several nanometers.

to achieve up to 0.001% absolute accuracy in isotopic abundance measurements of ^{13}C in a simulation of the C_2 Swan band with many resolved peaks, using eleven isotopic standards [59]. This study demonstrated the ability of PLS performance given spectral interference, and notes that atomic emission spectra which overlap molecular emission spectra in time and bandwidth serve to degrade the analytical performance of LAMIS [59]. The method discussed to determine isotopic abundance is a comparison of experimental data to spectra taken from samples of known composition [59], which is at the heart of this research. Further, the impact of interference peaks were analyzed, and a normalization procedure of determining the normalization factor in regions without interference peaks had best performance ultimately seeing 3‰ absolute variation for interfering peak intensities of three times that of the molecular band heads [59].

2.10.3 Neural Network Analysis (NNA).

NNA is a branch of machine learning that uses one or more successive or recursive algorithms to recognize patterns and build models describing the data [60, 58, 61]. It is loosely related to human learning in that, through repetition, a machine is able to make connections that allow classification, and even predictions. Each neural network "layer" is a collection of "nodes" which perform some mathematical operation on a data point from one or more nodes in the previous layer. Correction to the response of the combination of layers can performed in a number of ways. In this way the connections between layers are reinforced (weighted more heavily) where data provide closer approximations of the true data.

Artificial Neural Networks (ANN, one layer between the input data and output data) or deep neural networks (DNN, multiple layers between the input data and output data) can be trained to recognize (predict) non-linear behavior in datasets, where PCR and PLS cannot without data transformation. NNA has also been demonstrated to work as well as PLS in correcting for spectral interference as discussed above, and is in research as a potential analysis basis for calibration curve development in portable LIBS devices [58]. Other applications to LIBS data demonstrated RMSE values of 7% [62], but examples of NNA for classification of data are more prevalent [63, 58, 61].

III. Methodology

3.1 Experimental Setup.

Three different experiments were performed to test the ability of LIBS to quantitatively determine the concentrations of lithium isotopes. Low resolution experiments used a 350 mm McPherson spectrometer outfitted with a 1200 grooves per mm diffraction grating having a 700 nm blaze and a PiMAX2 ICCD. Medium resolution experiments were performed with a single stage of a Trivista 777 spectrometer (750 mm path length) and high resolution experiments with three stages of a TriVista 777 triple spectrometer (2.25 m path length) used in additive mode with successive 600, 600 and 1200 grooves per mm diffraction gratings copuled with a PiMAX4 gated ICCD. The laser used in all experiments was a Surelite Model I-10, frequency doubled (532 nm) Nd:YAG laser with a pulse width of 6 ns using laser energies of nominally 1,500 mW/pulse (see figure 6).

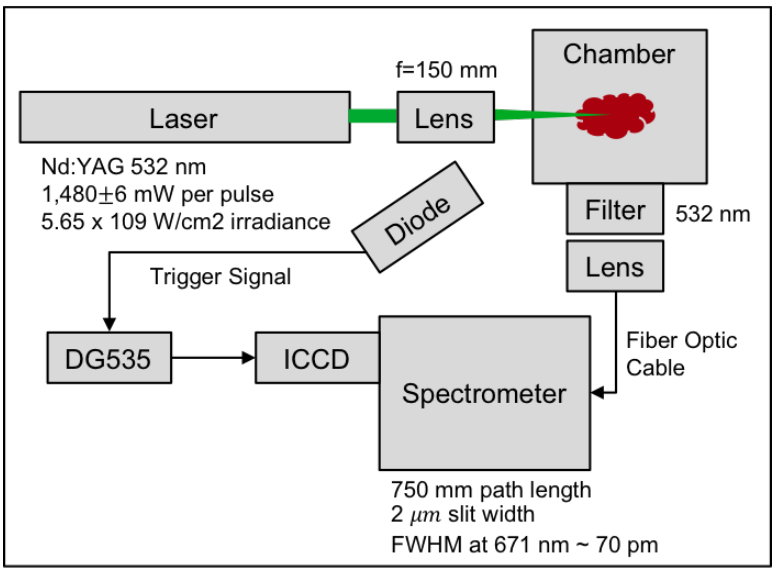

Figure 6. The experimental setup for low resolution experiments. The only change for medium and high resolution experiments was the change of the spectrometer to a TriVista 750 mm or model 777 (three 750 mm spectrometers linked in serial). In low and medium resolution, a DG535 delay generator was used to trigger the camera.

The laser was placed approximately one meter from the sample for convenience. The beam was focused by a 150 mm focal length lens and entered through a large fused-silica observation window onto the target located in a vacuum chamber, pumped down to nominally 40 mTorr (see figure 7). The Q-switch delay was set to 310 μs and

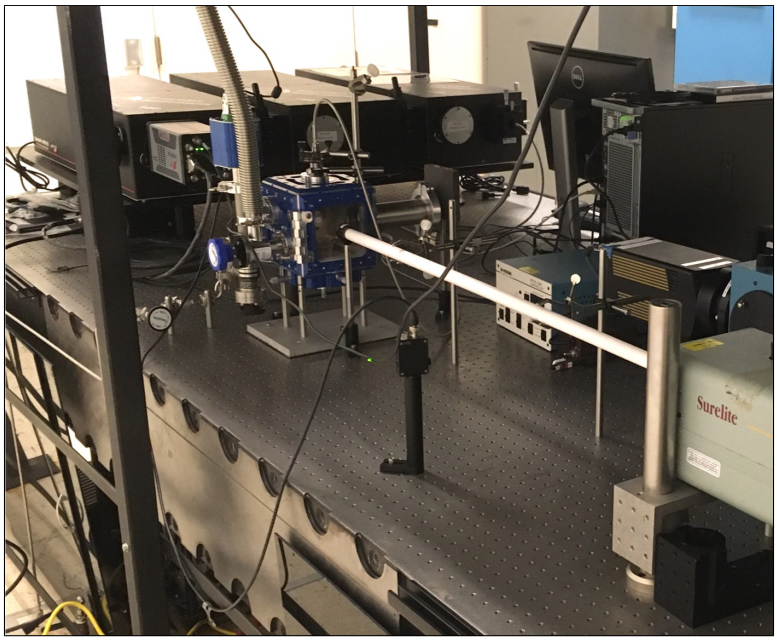

Figure 7. The experiment set-up on the table for medium and high resolution experiments only. The laser, bottom right in picture, fired through a PVC tube to the focusing lens, into the chamber through a large fused-silica viewing window. Reflected light was captured in the diode (center) which triggered the PiMAX4 camera (top left, behind cube). Light traveled out of the top of the cube through a 532 nm notch filter, into a 25 mm collimator which focused the light on a two meter, 19-fiber cable that carried the light to the spectrometer entrance slit (seen mounted top, right).

laser energy measured using a standard power meter. Light from plasma emission was captured through a 25 mm fused silica view port, a 532 nm notch filter and then a 25 mm collimator. It travelled to the spectrometer entrance slit through a 2 meter long fiber-optic cable with fibers stacked in a line at the end to match the slit geometry, which was aligned with the entrance port of the spectrometer. In low resolution experiments, a shutter was used to reduce noise by closely matching the slit length to the fiber optic cable output. In medium and high resolution experiments, noise reduct was accomplished through software, which limited the integrated signal on the

CCD to the fiber output (see figure 8). The entrance slit width of the spectrometer was consistently 1 or 2 μm.

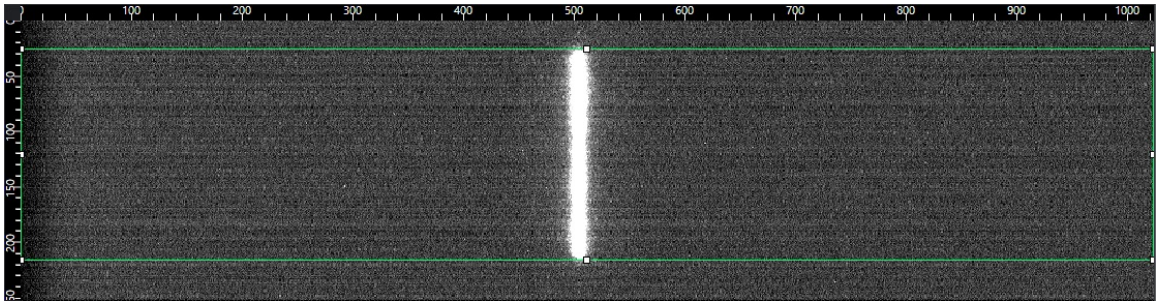

Figure 8. For medium and high resolution experiments, noise was reduced by integrated plasma emission signal only over the fiber stack. Here, the region of interest on the CCD is shown, demonstrating the limit of the signal taken from the fiber head. In the picture, the green box indicates the region of the ICCD that is used by the software to calculate the integrated intensity. In this case, the vertical range is limited to the output of the fiber optic stack, and the horizontal range (representing the bandwidth of measurement) is maximized. This adjustment serves to improve resolution by eliminating noise from the pixels that do not receive signal from the fiber stack.

For medium and high resolution experiments where the signal was software-limited as described above, the integrated intensity full width at half-maximum (FWHM) of lines produced by a neon lamp was measured by the LightView software to be on the order of 70 and 53 pm, respectively, in the spectral range of measurement (see figure 9). For context, this is more than four times the value of the isotopic shift measured in previous experiment [7]. In low resolution, the FWHM was measured to be 200 pm.

During all experiments, a laser diode placed between the laser and vacuum chamber determined pulse timing and trigger the ICCD. All ICCD gating was done through camera controller software and confirmed using a standard four channel oscilloscope. The timing set-up was evaluated for jitter in the camera trigger, and in the camera operation (see figure 10). Between shots, trigger timing deviation was found to be nominally below 1 ns, and deemed sufficient for expected gating needs.

Each sample face was placed on a sample stand at 45° to the laser beam and

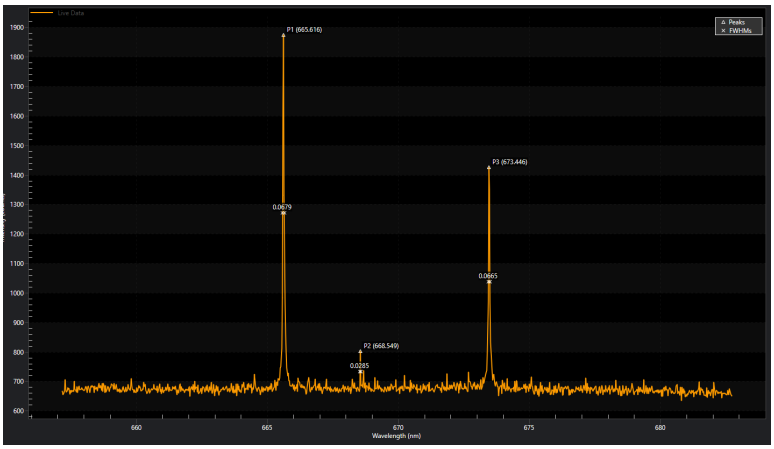

Figure 9. FWHM measurement of neon calibration lamp in the spectral region where the lithium doublet was measured. The FWHM value was roughly 70 pm, which is four times the value of the lithium isotopic shift measured previously [7].

Figure 10. This oscilloscope reading shows the general characteristics of the timing pulse created by the laser diode (3, top) and camera readout signal (4, bottom). Jitter between the diode trigger pulse to the camera, and the camera monitoring pulse was measured to be less than 1 ns shot to shot.

collimator for low resolution experiments, and perpendicular to the laser beam and at 90° to the view port for medium and high resolution experiments within a vacuum chamber (see figure 11). The chamber was sealed, purged with argon gas and then the internal pressure was reduced. Due to the monohydrated material, very low vacuum was not possible, but vacuum of 40 mTorr was reliably maintained throughout data

collection.

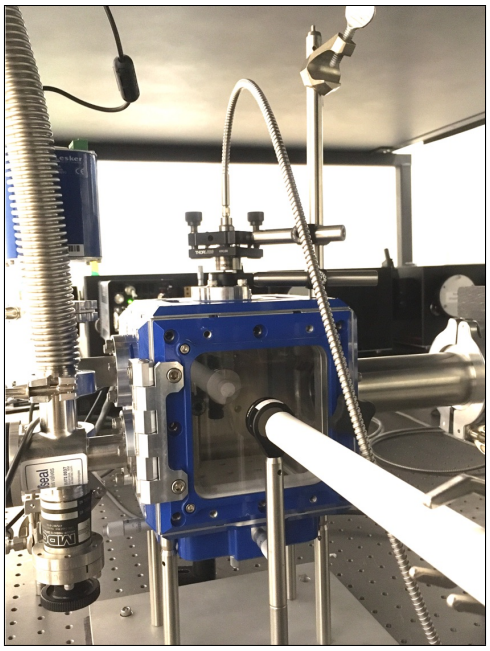

Figure 11. IdealVacuum vacuum chamber used for all experiments, with sample mounted inside. The bottom contains an XYZ translation stage. The laser entered a large, fused-silica window, and was collected through the light collimator can seen mounted at the top. A 532 nm notch filter was used to protect the camera from laser light.

3.2 Sample Preparation.

Samples were prepared from Sigman-Aldrich lithium hydroxide monohydrate (99.9% pure 95% $^{6}LiOH{\cdot}H_2O$ and 97% $^{7}LiOH{\cdot}H_2O$) powders and mixed using standard laboratory equipment. Powders were milled in an agate mortar and pestle by hand and pressed with a one cm diameter stainless steel die at 7.8 kPSI for 60 seconds (see figure 12). No binder was used and the sample was adhered to a sample stand using Elmer's brand rubber cement or transparent tape between the backside of the sample and the sample stand. The measured masses of mixed stocks were used to calculate isotopic concentrations.

Sample concentrations were chosen to provide even spacing from highly enriched

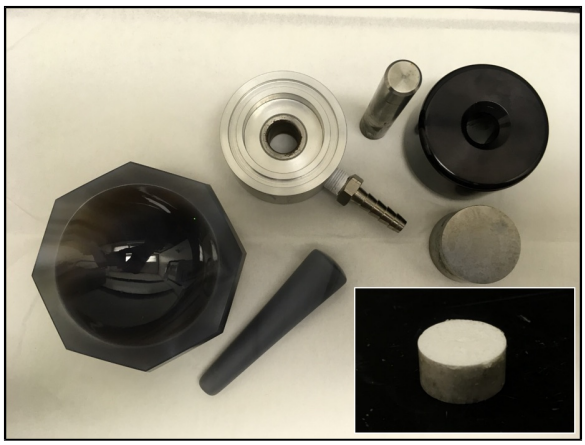

Figure 12. Sample preparation tools and pressed sample (inset). The mortar and pestle is made from agate. The pressing die is stainless steel. Dimensions of the final samples were 1 square inch on the face, and approximately one-half inch tall. Each was pressed from approximately 1.5 grams of crushed powder, pressed at 10 kPSI for 60 seconds.

to highly depleted mixtures (see figure 13).

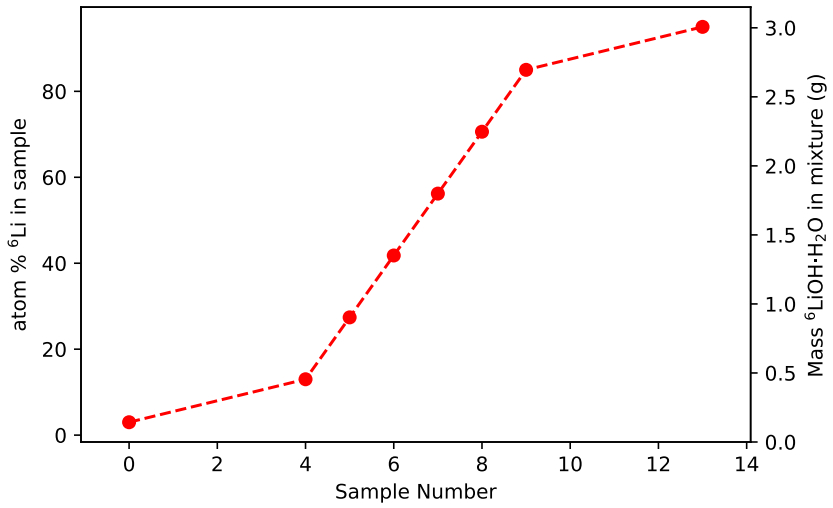

Figure 13. Graphical depiction of concentrations to be measured. Closer spacing was used from 1% to 11% of each isotope to provide better fidelity in measuring the limit of detection in highly enriched and depleted mixtures.

The sample was ablated with laser pulses directly impinging on the face of the sample in up to 3,000 laser shots. Between 100 and 300 spectra were collected for each resolution experiment, where each spectra was a cumulative collection of between 10 and 30 laser ablations. The sample was periodically moved using the integrated

XYZ translation stage to avoid plasma shielding due to deep holes in the sample. It generally took between one and five minutes to collect the spectra from a sample, depending on how often the sample was moved.

3.3 Post-processing.

Following collection of each dataset, a range of pixels about the lithium line at 670.8 nm were selected to improve model performance. The background was removed from each spectrum by subtracting its lowest value in the reduced spectra. The background-subtracted spectra were then normalized by dividing all recorded values by the peak intensity value in the reduced spectra, and smoothed using a Savitsky-Golay filter.

In medium resolution experiments, that data was passed into a Python algorithm to detect and remove outliers using the minimum covariance determinant estimator. This technique is applied by finding the smallest covariance determinant (geometrically the volume scaling factor) from several random subsets of samples from within the sample space to determine a least-polluted subset. Once found, the Mahalonobis distance was calculated. This distance is equivalent to the Euclidian distance normalized to a multi-dimensional distribution's standard deviations [64, 65].

Once outliers were removed, an equal number of sample spectra were collected from each concentration to form a balanced set of data, separated into a training set (75% of data) and a test set (25% of data). Data were mathematically transformed to fit a standard-normal distribution and then passed to chemometric analysis algorithms developed as part of this thesis. This transformation allowed evaluation of over-fitting and model stability.

To validate the operation of code produced to perform chemometric analysis, a simulation of spectra was produced and passed into the PCR, PLS and DNN algo-

rithms for analysis. Simulated data was produced by adding two weighted, noisy Gaussian curves of 16 points (see figure 14). The peaks were placed at adjacent points, and the data were normalized in the same way as experimental data - the lowest value in the spectrum subtracted, then normalized to their peak intensity, then transformed to a standard normal deviation. The noise contribution was set to 10% of peak intensity, and the weights summed to one. Weights in this case were meant to represent the fraction of the sample that contained each peak and the noisy Gaussian curves to represent the spectrum of either ^{6}Li or ^{7}Li.

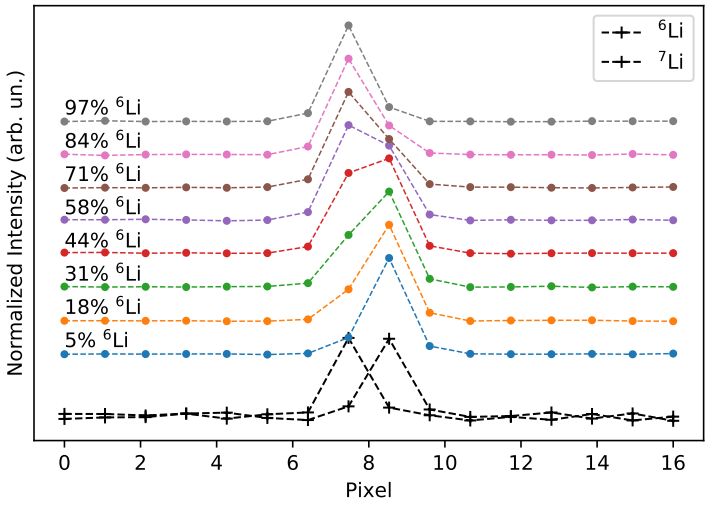

Figure 14. Simulated data used to test chemometric method algorithms developed in this research. The data represent the summation of two noisy Gaussian curves (bottom), weighted by their fractional concentration (vertically offset for clarity).

3.4 Analysis of Residuals and Variance.

Treating each sample as an experiment in its own right allowed within-sample variance to be characterized, which is useful as the eight hundred spectra collected for each data point may be affected by matrix effects, jitter, etc. Analysis of this variance allowed characterization of the precision of the experimental setup to inform

efforts to improve systematic error.

Ultimately this experiment was established as a randomized complete block design (RCBD) with each sample considered a unit, and blocking for statistical analysis performed on administrative data for preparation and data collection. By blocking in this fashion, systematic error could be traced to sample preparation methods (sample order, shot order, sample mixing date), or the experimental variables in the ablation (laser power stability, atmosphere, experimenter, etc.).

Toward this end, data was analyzed using the software package R to ensure statistical features were observed, namely that within blocks residuals are normally distributed about zero and that nuisance factors (experimental variables not optimized) do not have a significant effect on the results. This analysis allows further assessment of the accuracy and completeness of the model. Tools used were plots of residuals versus fitted values, residual quantiles versus normal quantiles, residuals versus leverage and scale versus location.

IV. Results

This section describes the results of the analysis performed on simulated and experimental data by all three chemometric methods. R^2, RMSE and prediction results are those taken from cross-validation data only (i.e. not the data used to create the prediction model).

4.1 Simulations.

The results of two simulations described previously are presented in this section. The simulation of atomic emission spectra was performed to test the chemometric analysis techniques presented below and the simulation of molecular spectra was performed to inform LAMIS measurement.

4.1.1 Atomic Emission Spectra.

Using the data from this simulation (see figure 15) chemometric algorithms were applied to 75% of each sample's data to create a model, and that model was applied to the remaining 25% of data to predict the concentration for ^{6}Li in the sample, from which root mean squared error (RMSE) and R^2 were calculated to assess the ability of the algorithm to produce an accurate model of the spectral data.

4.1.1.1 PCA.

The PCA algorithm achieved a minimum RMSE of 0.0389 from the absolute atom fraction of known sample concentrations of ^{6}Li using fifteen principal components (see figure 16), which was coupled with an R^2 statistic of 0.9833. These fifteen components explain roughly 97.5% of the variance in the spectra (see figure 17).

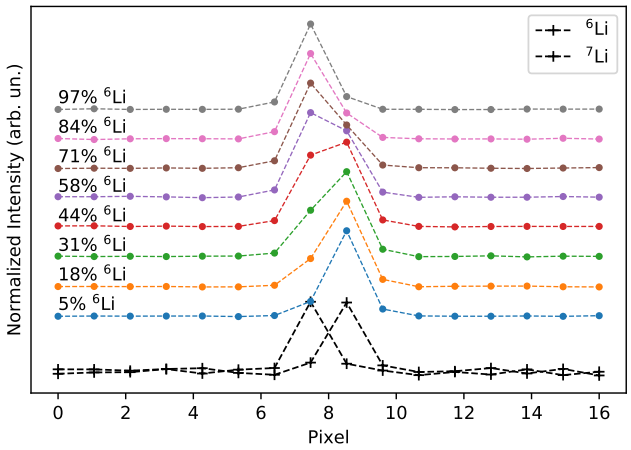

Figure 15. Simulated spectra used to test the performance of chemometric algorithms developed for this thesis, vertically separated for clarity. 100 normalized spectra of eight combinations were generated assuming that the spectrum of each combination is a linear combination of the concentrations of isotopic lithium hydroxide, where the spectral peak between isotopes was modeled to be one pixel (i.e. 5% ^{6}Li would be the summation of the ^{6}Li peak at 5% intensity and the ^{7}Li peak at 95% intensity. Random noise was also added.

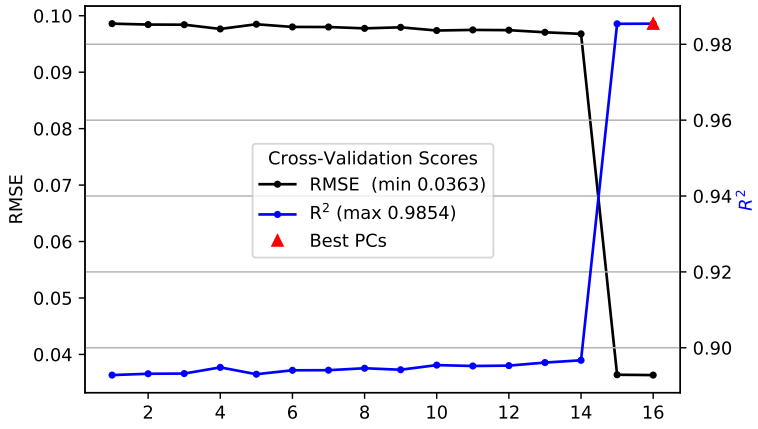

Figure 16. RMSE and R^2 plots for PCA on the simulated data. Optimum RMSE 0.0389 is achieved at 15 principal components, which yields a R^2 parameter of 0.9833.

Moderate separation between clusters was observed in the PCA scores plot in three dimensions (see figure 18), and a trend for separation along all three PCs for changing ^{6}Li concentration is not readily apparent.

Linear regression on PCA predictions produce a very good fit to an ideal line, and

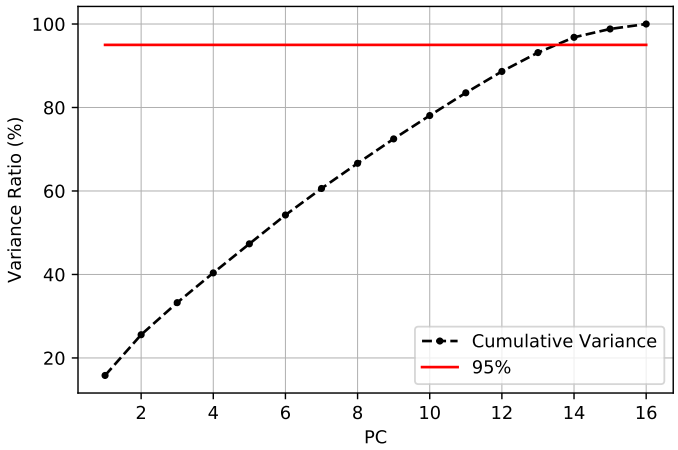

Figure 17. Cumulative percentage of variance explained by the principal components versus number of PCs (x axis). 95% variance indicated by a red line. With sixteen principal components, 100% of variance is explained.

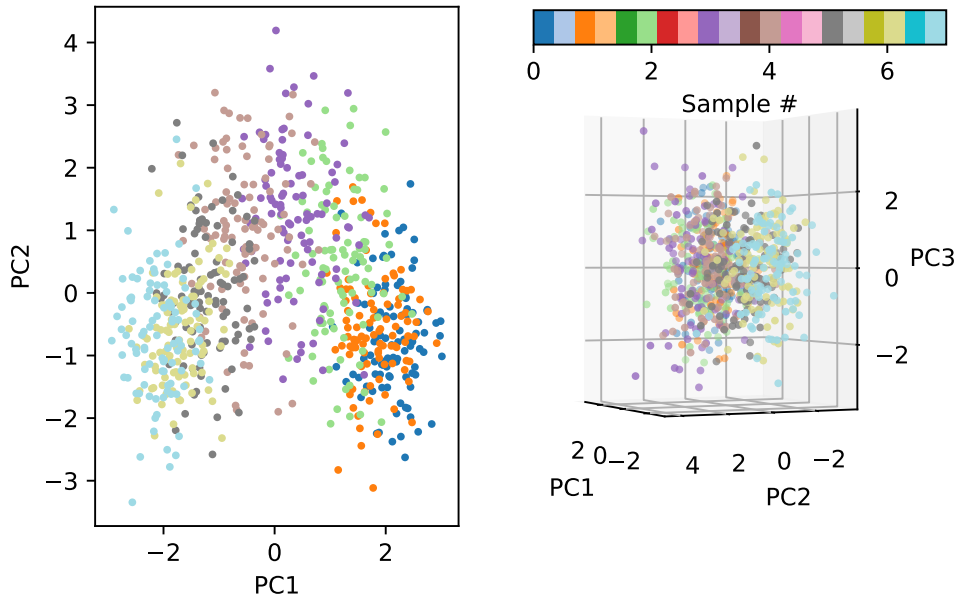

Figure 18. Plot of all 16 PCs from PCA analysis of simulated data. Note the colors are indicative of sample number, which is tied to ^{6}Li concentration (the higher the sample number, the higher the concentration of ^{6}Li). Separation of clusters is not apparent in 2 or 3 dimensions.

yield model predictions that are indicative of the actual values. Model predictions are clearly separated in values, as one standard deviation ranges do not overlap between

concentrations (see figure 20). Three representations of the data are presented simultaneously for each method in this plot. For each concentration of ^{6}Li, the prediction means and root mean squared error for cross-validation data are represented centered on the concentration value, while the predictions are shown offset right, and a box plot with whiskers to 1.5 interquartile ranges offset to the left.

4.1.1.2 PLS results.

The PLS algorithm with just 5 features, achieved a minimum RMSE of 0.0389 from the absolute atom fraction of known sample concentrations of ^{6}Li identical to PCA (see figure 19), which was coupled with an R^2 statistic of 0.9833.

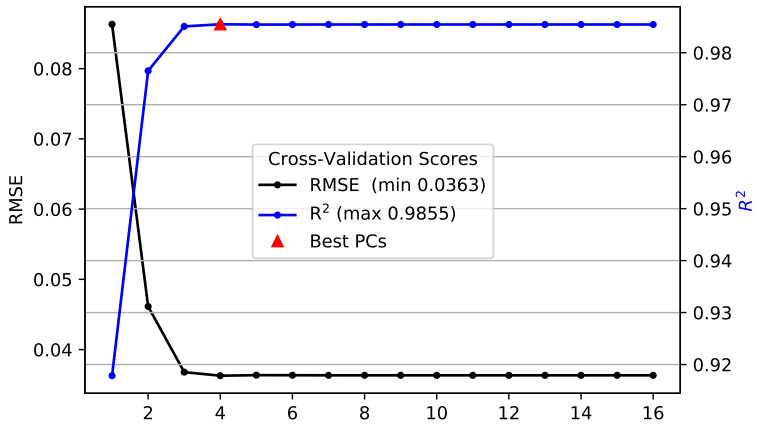

Figure 19. RMSE and R^2 plots for PLS on the simulated data. Optimum RMSE 0.0389 is achieved at just 5 features, which yields a R^2 parameter of 0.9833.

As with PCA, linear regression on PLS predictions produce a very good fit to an ideal line, and yield model predictions that are indicative of the actual values. Model predictions are clearly separated in values, as one standard deviation ranges do not overlap between concentrations (see figure 20).

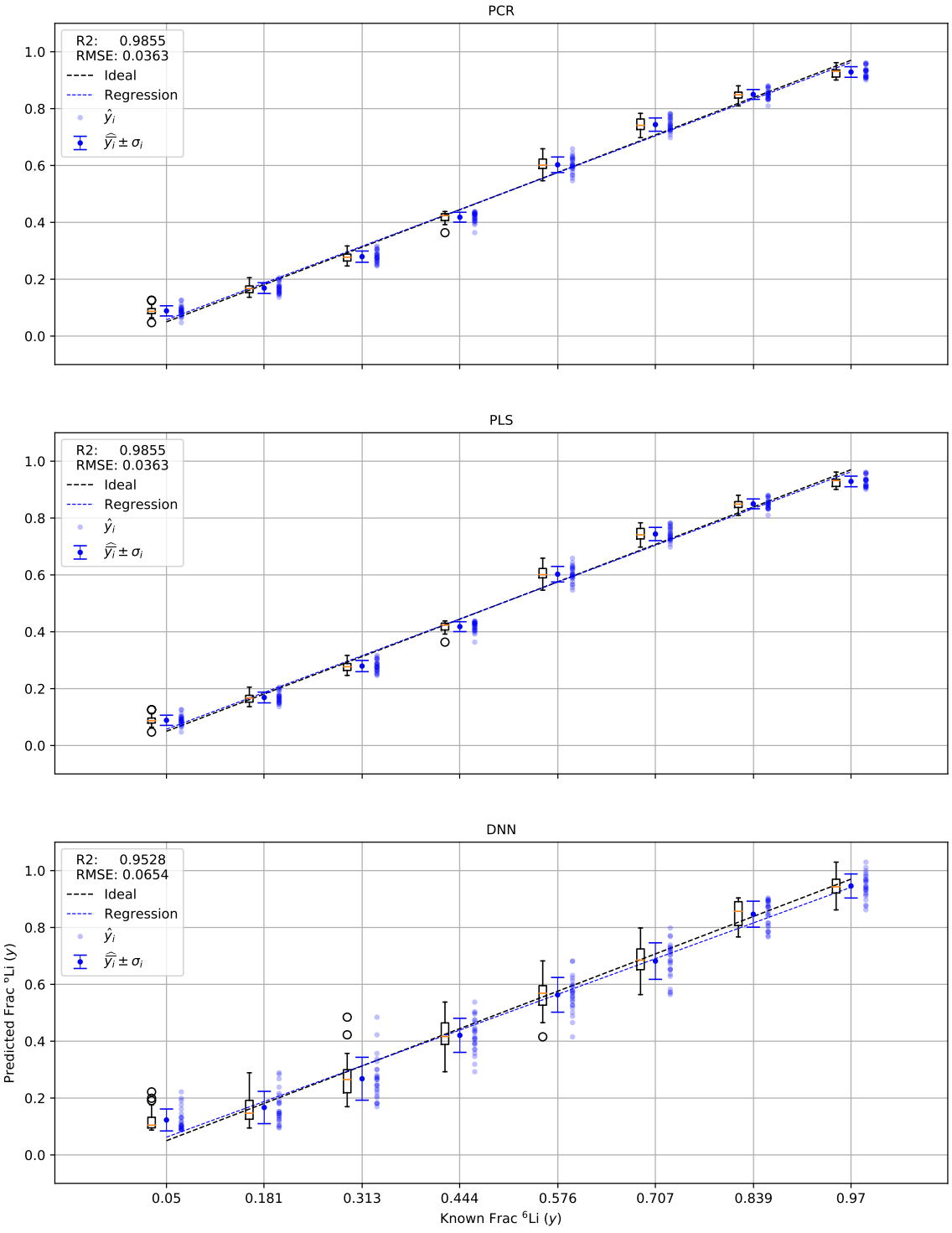

Figure 20. Regression plots for chemometric methods applied to simulated data. For each concentration of ^{6}Li, prediction means and standard deviation are represented centered on the concentration value, predictions are shown offset left, box plot with whiskers to 1.5 interquartile ranges offset the right. RMSE and R^2 indicated in the legend. All three methods were found to perform very similarly.

4.1.1.3 DNN results.

A DNN algorithm using three hidden nodes achieved a minimum RMSE of 0.0559 from the absolute atom fraction of known sample concentrations of ^{6}Li. This is similar but slightly worse performance that PCA and PLS, which was coupled with an R^2 statistic of 0.9655 (see figure 20).

As with PCA and PLS, linear regression on DNN predictions produces a very good fit to an ideal line, and yield model predictions that are indicative of the actual values. Model predictions are clearly separated in values, but one standard deviation ranges overlap between the most extreme concentrations (see figure 20).

4.1.2 Model Comparison.

Taken together this demonstrates that all algorithms developed for this work are sufficient to the task of finding patterns in spectral data.

4.2 Experimental Data

Low resolution LIBS experiments were performed to demonstrate the ability of the experimental set-up to perform LIBS and allow training with the equipment. The data taken were not analyzed to produce a calibration curve. For medium resolution LIBS, this section follows the same arc as the analysis of simulated atomic spectra above. For high resolution LIBS, the SNR of data were not sufficient to allow for analysis by this method as spectra were noise dominated.

4.2.1 Low Resolution LIBS.

Samples were ablated inside of a low pressure, argon-backfilled chamber with the laser incident, and light collected, at a 45° angle to the sample. The laser pulse was nominally 1,500 mW with a 6 ns pulse width, and produced a spot size of approxi-

mately 725 μm in diameter when focused through a lens with 150 mm focal length (see figure 21). Using an optical microscope, the sample appeared to have crystalline structure with cross-grain areas showing as darker areas when backlit. Additionally, the craters appeared oblong, indicating the laser was not impinging on the sample at a perfectly perpendicular angle.

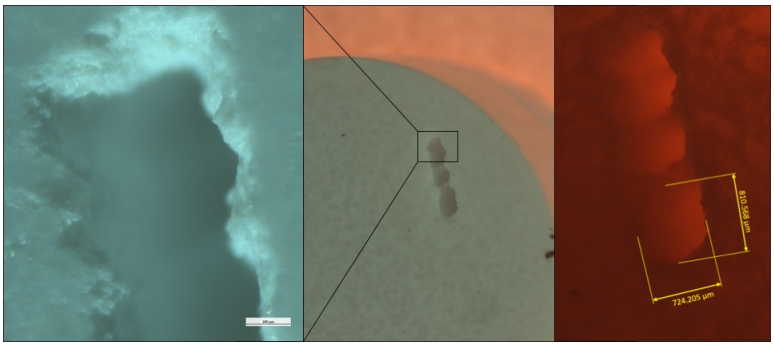

Figure 21. Craters after ablation (center, top lit sample). Edges of the craters are shown with some crust observed (left, obliquely lit sample) as expected from ns pulsed laser ablation [28] and the spot size is measured to be 725 μm (right, backlit sample). It is apparent that the laser was not absolutely perpendicular to the sample, and the crystalline structure of the sample can be observed where darker areas are believed to be cross-grain structure to that of the lighter areas believed to be end-grain structure [66].

300 spectra consisting of the summation of 30 individual shots were collected using a 350 mm monochromator, and a gate delay of 215 ns with a gate width of 500 ns was used determined to maximize SNR. ICCD gain was set to 130/255.

Post-processing, to include background subtraction, normalization and smoothing, was applied to each spectra, but no outlier rejection was performed in processing low resolution experimental data. FWHM and center wavelengths were determined via a Voigt profile fit using the LMFIT package for Python. Figure 22 shows the Stark shift over time, with the largest shift at very early time. Stark broadening was determined to be at least on the order of 0.4 nm, making full peaks for each isotope unresolvable in the traditional sense.

The isotopic shift between the peaks of ^{6}Li and ^{7}Li was measured to be 28 $\pm$ 2 pm,

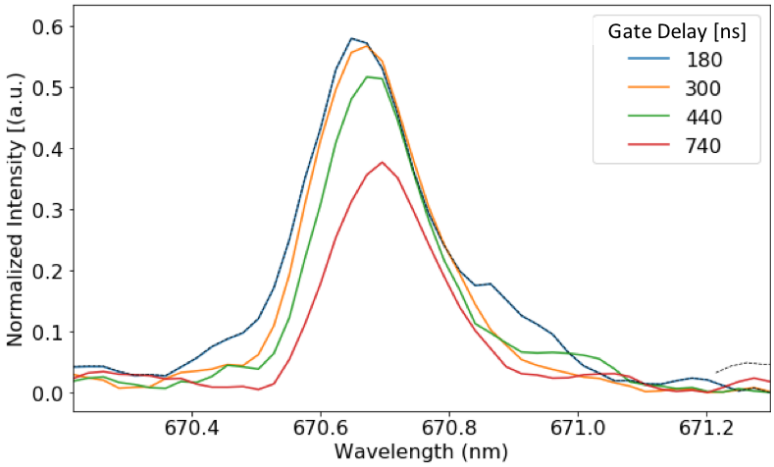

Figure 22. Stark shift over time shown in 0.95% ^{7}LiOH·H_2O with the gate delay indicated by color. The gate width for all spectra is 120 ns. At early times (180 ns) the peak is blue-shifted from the expected high intensity doublet at 670.725 nm [49].

and at a slightly higher wavelength than previously reported [7] due to measurements taken when the plasma was still very hot and prone to Stark shift. The isotopic shift is 11 pm larger than measured in previously published results [7] (see figure 23).

4.2.2 Medium Resolution LIBS.

Samples were ablated inside of a low pressure, argon-backfilled chamber with the laser incident and light collected at a 90° angle to the sample. The laser pulse was nominally 15 mJ with a 6 ns pulse width, and produced a spot size of approximately 725 μm in diameter when focused through a lens with a 130 mm focal length (see figure 21). 100 spectra of 10 on-CCD accumulations were collected using a 750 mm monochromator, a gate delay of 1 μs and a gate width of 1 μs . ICCD gain was set to 1/255.

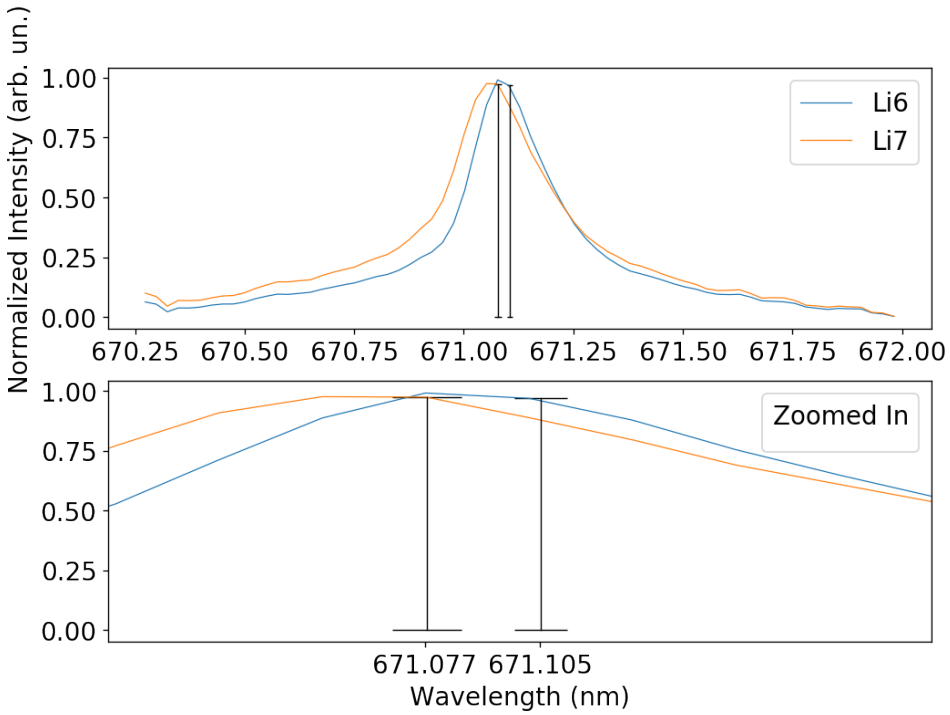

Figure 23. Isotopic shift of ^{6}Li and ^{7}Li measured in this research. Each spectrum is the average of 300 spectra each taken as the summation of 30 on-CCD accumulations, a gate delay of 250 ns and a gate width of 500 ns. The shift in atomic emission spectra was found to be 28 $\pm$ 2 pm.

4.2.2.1 Experiment Optimization, Postprocessing and Outlier Rejection.

Inspection of time evolved atomic emission spectra showed that SNRs were best in the 1-2 μs time window. As an example, data from this research is shown in figure 24, which shows ten spectra taken in 1 μs gate widths with gate delays advancing from one to ten microseconds.

The average emission spectra for select concentrations are shown in figure 25. Spectral differences that may allow for discrimination of concentrations are observable just off peak (see inset of figure 25). These suggest the two unresolved peaks of ^{6}LI and ^{7}Li fall within the bounds of these pixels.

The maximum normalized shot-to-shot intensity of each point on the curve varied

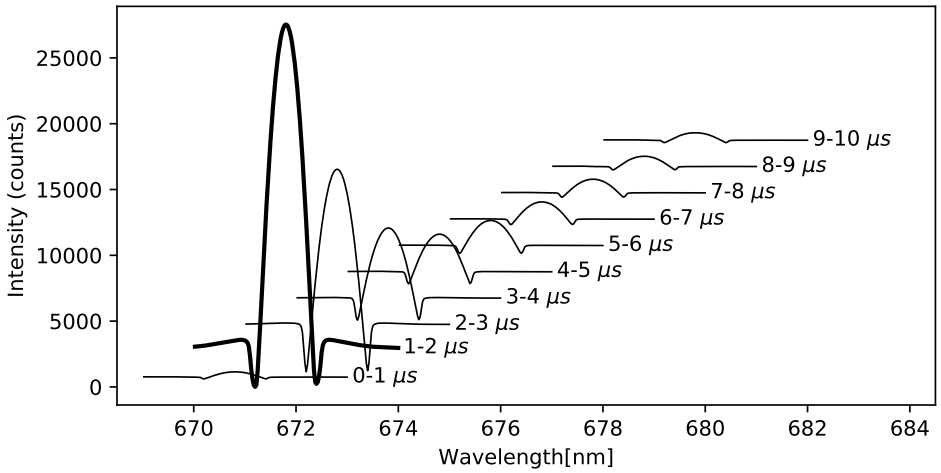

Figure 24. Typical measurement of atomic emission spectra over time used to optimize the gate delay and width, with background subtracted by collection software. Each spectrum shown in this plot is produced from 10 accumulations each over a 1 μs gate width. They are taken every 1 μs beginning with 0.025 μs (bottom) through 10.025 μs (top). The greatest SNR is between 1-2 μs.

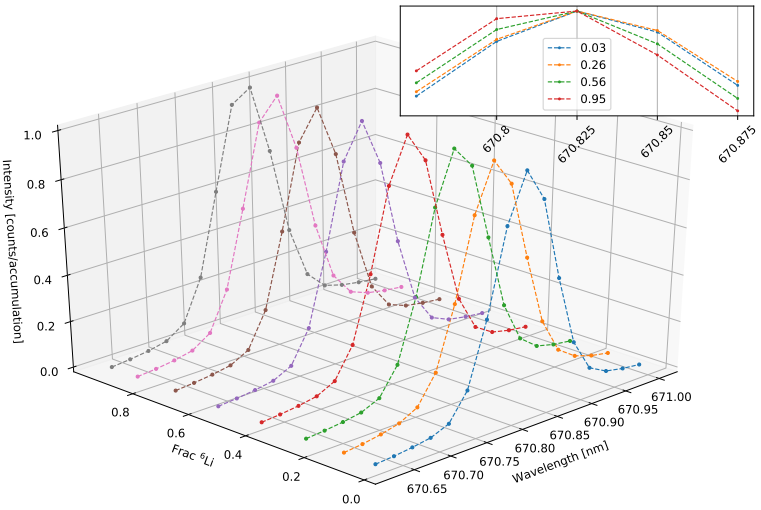

Figure 25. The average emission spectra by concentration. The inset plot highlights the 0.03, 0.26, 0.57 and 0.95 ^{6}Li fraction samples' features surrounding the peak intensity. Note the shift of intensity from right of peak to left of peak increasing with ^{6}Li fraction.

from 0.0568 to 0.1141 (see figure 26). A pattern is apparent as samples with lower concentrations of ^{6}Li have a peak shifted to lower wavelengths, and vice versa. This pattern is useful for chemometric techniques that use variance between features in a

spectra to develop a model of predictions, and the more consistent behavior within the sample, the higher accuracy the model can achieve.

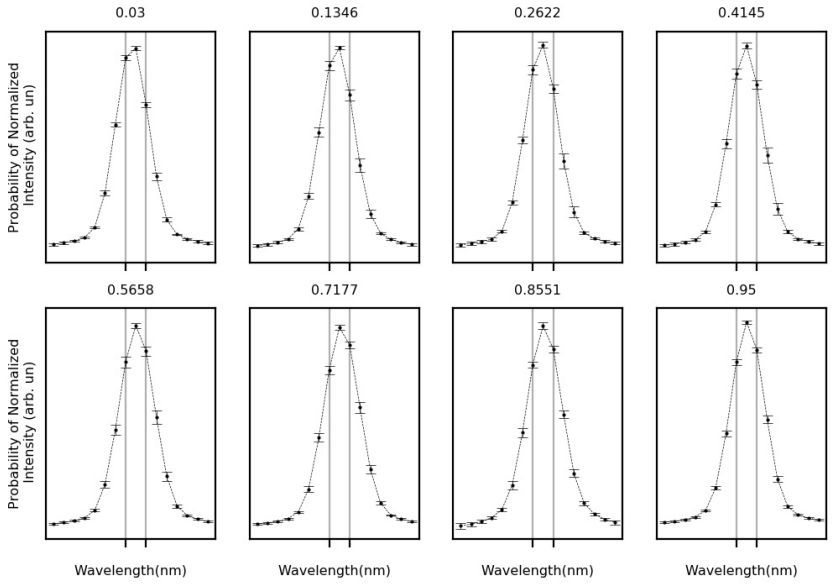

Figure 26. Shot to shot variation for each sample concentration as labelled at top of chart. Vertical lines represent lines at 670.80 and 670.85 nm for reference. Raw data has been normalized to peak intensity, background subtracted, and transformed to a standard normal distribution - this is the state of the data being used by the chemometric algorithms. The unmixed samples are the most stable with the 0.03 and 0.95 ^{6}Li fraction samples having maximum standard deviations of 0.0568 and 0.0571, respectively by comparison to the highest of 0.1141 in the 0.4345 ^{6}Li fraction sample.

After preprocessing the data with normalization and background-subtraction, outliers were identified using the MCD method as previously described (results in table 2). Variation in intensity led some spectra in highly enriched $^6LiOH{\cdot}H_2O$ to be noise dominated owing to the lower intensities observed in high concentration ^{6}Li, or inhomogeneous mixing in samples with similar ratios of isotopes. 12 outliers were chosen (out of 100 spectra) in the 0.95 atom fraction ^{6}Li, and the outliers can be seen in figure 27. Following outlier rejection, 88 spectra were selected from each concentration to form a balanced sample set.

Concentration	Outliers Removed
0.030000	10
0.134586	2
0.262197	6
0.565850	1
0.717737	1
0.855138	1
0.950000	12

Table 2. Outliers selected using MCD technique. Variation in intensity led some spectra in highly enriched $^{6}LiOH{\cdot}H_2O$ to be noise dominated owing to the lower intensities observed in high concentration ^{6}Li, or inhomogeneous mixing in samples with similar ratios of isotopes.

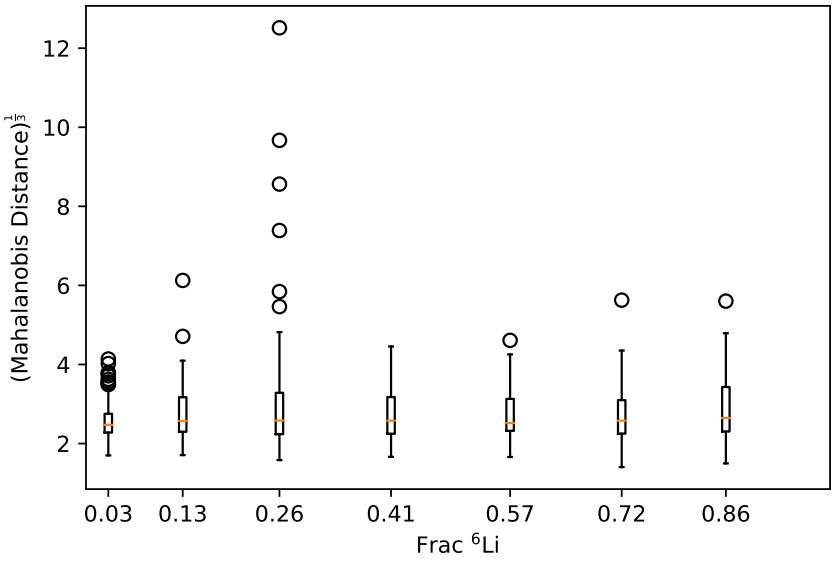

Figure 27. Outliers selected based on minimum covariance determinant method of selection. The Mahalanobis distance is equivalent to Euclidean distance normalized to a multi-dimensional distribution's standard deviations. This shows the distance a point lies from the mean of its distribution, taken across the 16 pixels making up the normalized spectra. Outliers shown are more than 1.5 interquartile ranges beyond the first or third quartiles. The greatest fraction of outliers were found in the 0.95 ^{6}Li fraction sample, at 12 of 100.

4.2.2.2 Chemometrics.

With the data normalized and outliers rejected, the spectra were passed into chemometric analysis algorithms developed as part of this thesis. Inside of each algorithm, each spectra was transformed to a standard normal distribution, but were not otherwise altered between algorithms.

	PCA Prediction		PLS Prediction		DNN Prediction	
^{6}Li Fraction	$\tilde{y} \pm \sigma$	% $(100\times\sigma/\tilde{y})$	$\tilde{y} \pm \sigma$	% $(100\times\sigma/\tilde{y})$	$\tilde{y} \pm \sigma$	% $(100\times\sigma/\tilde{y})$
0.0300	0.0242 ± 0.0503	207.9533	0.0194 ± 0.0463	238.2072	0.0666 ± 0.0279	41.8651
0.1346	0.1846 ± 0.1014	54.9290	0.1919 ± 0.0984	51.2794	0.1512 ± 0.0701	46.3763
0.2622	0.3314 ± 0.0767	23.1533	0.3317 ± 0.0709	21.3684	0.3558 ± 0.0952	26.7597
0.4145	0.4273 ± 0.0819	19.1583	0.4281 ± 0.0802	18.7354	0.4372 ± 0.1130	25.8552
0.5658	0.6391 ± 0.0735	11.5058	0.6402 ± 0.0785	12.2697	0.6667 ± 0.0863	12.9420
0.7177	0.7849 ± 0.0972	12.3824	0.7734 ± 0.0950	12.2783	0.7474 ± 0.0692	9.2583
0.8551	0.8144 ± 0.0839	10.2985	0.8267 ± 0.0861	10.4167	0.8660 ± 0.0812	9.3783
0.9500	0.7241 ± 0.0585	8.0736	0.7186 ± 0.0639	8.8862	0.8206 ± 0.0908	11.0699

Table 3. Prediction means and error for chemometric models. Absolute error is greatest in PCA and PLS for mixed samples, and generally less everywhere for the DNN. This suggests a non-linear pattern in the data that is better found by the DNN than the linear methods of PCA and PLS.

The results of regression can be seen in figure 28. Results from the three chemometric approaches are presented simultaneously. For each concentration of ^{6}Li, the prediction means and standard deviation are represented centered on the concentration value, while the predictions are shown offset right, and a box plot with whiskers to 1.5 interquartile ranges offset to the left. Table 3 provides the means, standard deviations and percent error for each method and sample concentration.

PCA with five PCs and PLS with four features performed similarly, achieving a RMSE of 0.1217, 0.1220 and R^2 fits of 0.8516, 0.8508 respectively. Since the DNN is initialized by random weights vectors in each layer, analysis of R^2 and RMSE was performed 100 times to attain an average measure of performance. The DNN RMSE was 0.110±0.0056 and R^2 0.88±0.0127, where RMSE is marginally better than those of PCA and PLS. PCA and PLS weights given in Table 4.

w_i	PCA	PLS	w_i	PCA	PLS
w_0	0.0954	0.0000	w_8	0.0301	0.0000
w_1	-0.0311	0.0006	w_9	0.0152	0.0166
w_2	0.0418	-0.0326	w_{10}	-0.1075	0.1959
w_3	0.0164	0.0554	w_{11}	0.0918	-0.1566
w_4	0.1261	0.0726	w_{12}	0.1004	-0.0339
w_5	0.0195	-0.1250	w_{13}	-0.1919	0.0890
w_6	-0.1323	-0.1214	w_{14}	-0.0000	0.0165
w_7	-0.0035	-0.0231	w_{15}	0.0000	-0.0366

Table 4. PLS and PCA regression weights from linear model fitting. All values are shown, not only the values given for the best fit. x_i are the weights given to the corresponding pixel (indexed to zero) in determining the predicted value.

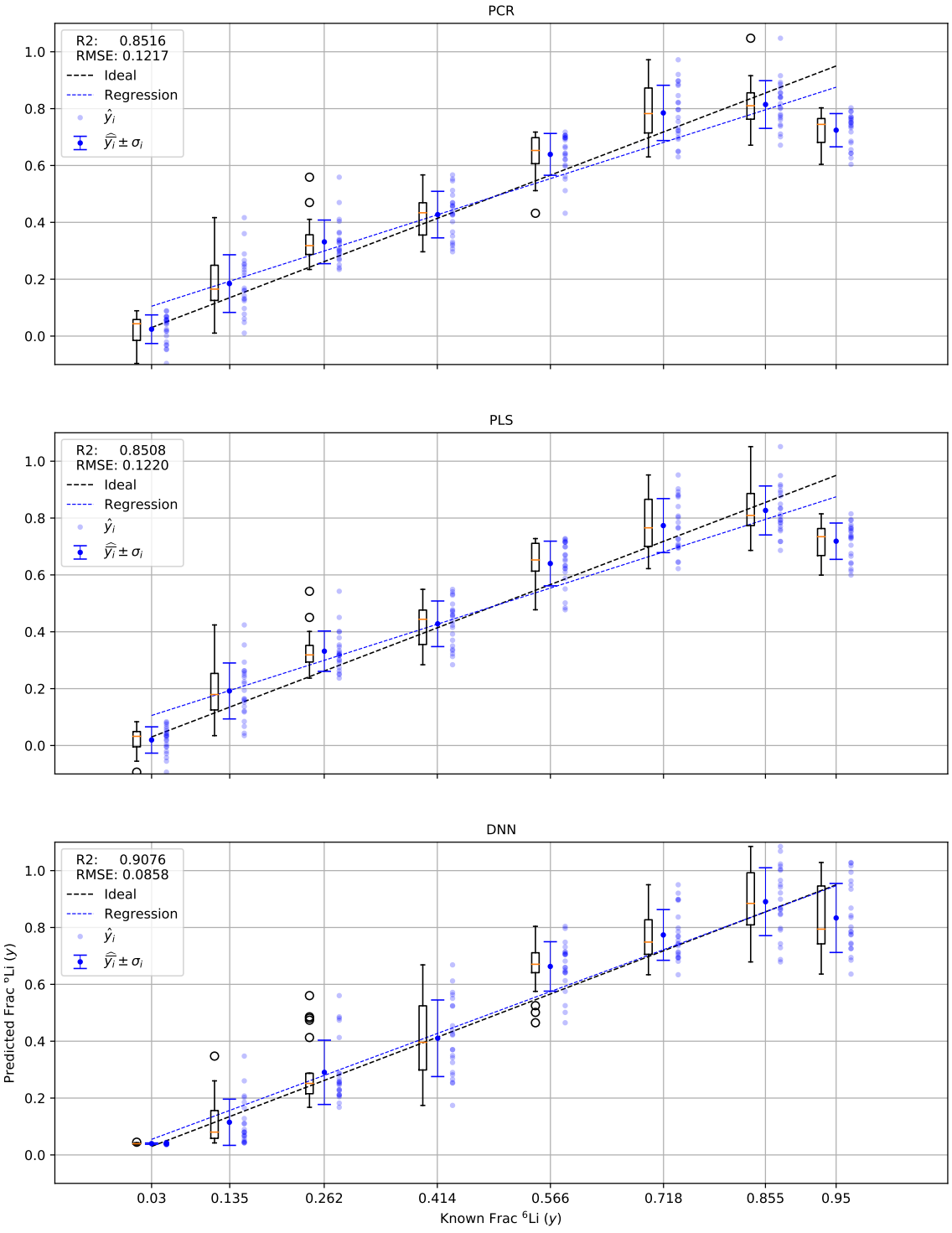

Figure 28. Regression results for PCA, PLS and DNN. Three representations of the data are presented simultaneously for each method. For each concentration of ^{6}Li, prediction means and standard deviation are represented centered on the concentration value, predictions are shown offset left, box plot with whiskers to 1.5 interquartile ranges offset the right. The DNN performs better than does PCA or PLS in both R^2 and RMSE.

The DNN was optimized without an exhaustive search of parameters to use eight hidden layers (10 layers in total counting the input and output layers) with nodes as show in table 5. Each layer was activated by a rectified linear unit and weights were initialized using a normal distribution (kernel).

Layer type	Output Nodes
Input	16
Hidden 1	32
Hidden 2	64
Hidden 3	128
Hidden 4	256
Hidden 5	256
Hidden 6	128
Hidden 7	64
Hidden 8	32
Output	1

Table 5. DNN model summary. The output nodes double for each layer from 1st to 4th hidden layer, and then reduced by half for each layer from the 5th to the 8th hidden layers, ultimately producing one value as a prediction.

4.2.2.3 Analysis of Residuals.

Residual analysis was performed to ensure completeness and adequacy of each model. By observation (see figure 29), the residuals of the PCA predictions are not distributed about zero, which suggests that the model is at least incomplete. The Normal QQ (theoretical quantiles vs actual quantiles) plot shows that residuals deviate slightly from a normal distribution. The Residuals vs Fitted plot shows a pattern of residual distribution with ^{6}Li fraction, and the Scale-Location plot shows that the variance of residuals changes slightly as well. Residuals vs Leverage shows that no outliers remain that should significantly affect the model, which is indicated by Cook's distance [67], which would appear on this plot as a dotted isoline if such a change were evident.

Similarly, PLS predictions show much the same phenomena (see figure 30) - a near normally distribution of residuals, a pattern in residuals centering, variance changes slightly over concentration and no significant outliers.

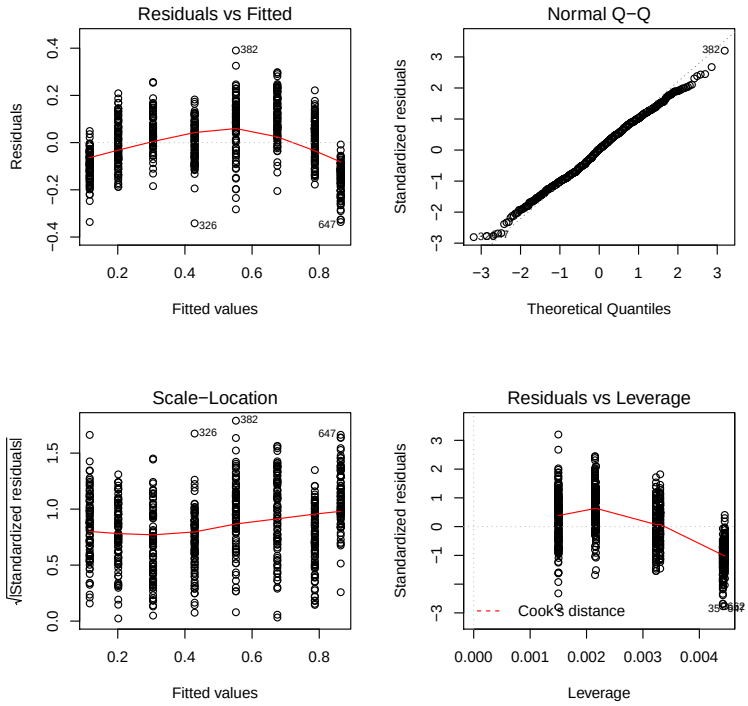

Figure 29. Residual plots for PCA results performed on experimental data. The Normal QQ plot shows a nearly normal distribution of residuals. The residuals vs fitted plot shows a pattern of residual distribution with ^{6}Li fraction, and the Scale-Location plot shows that the variance of data changes slightly as well. Residuals vs Leverage shows that no outliers remain that should significantly affect the model.

DNN predictions show much the same phenomena (see figure 31) as the previous two with some deviation. A "kink" and deviation from the extremes of the theoretical quantiles suggests even less normally distributed residuals, while the other plots show the same phenomena discussed above.

4.2.2.4 Linear Fit Statistics and Analysis of Variance.

Before analysis of variance, linear fit statistics were evaluated to determine the significance of the slope and intercept values, which were found to be significant for all models (see table 6). This is not unexpected considering the goodness of the fit parameters.

An analysis of variance was performed on the data to determine model complete-

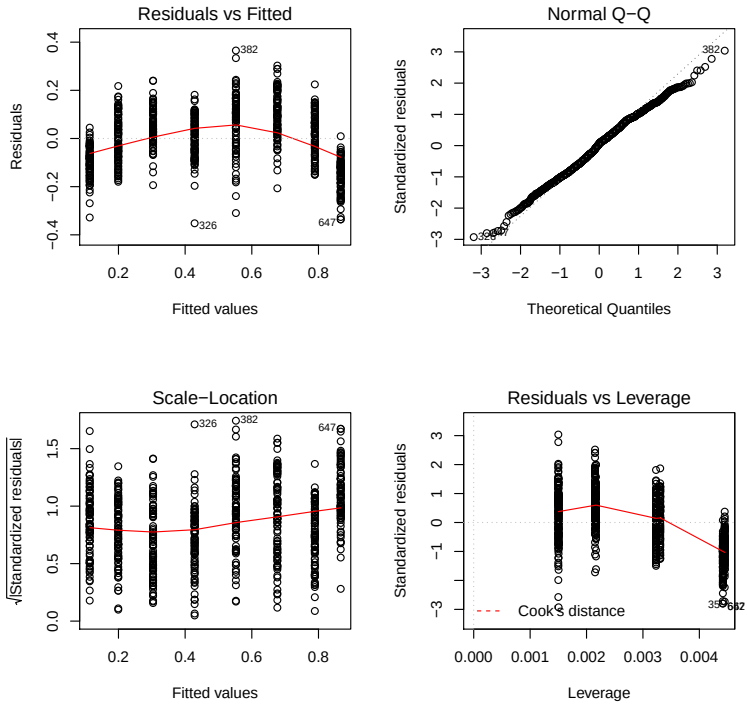

Figure 30. Residual plots for PLS results performed on experimental data. The Normal QQ plot shows a nearly normal distribution of residuals. The residuals vs fitted plot shows a pattern of residual distribution with ^{6}Li fraction, and the Scale-Location plot shows that the variance of data changes slightly as well. Residuals vs Leverage shows that no outliers remain that should significantly affect the model.

Model	Coefficient	Estimate	Std. Error	t value	Pr(>|t|)	Sig
PCA	(Intercept)	0.092079	0.008497	10.84	<2e-16	***
	y	0.812561	0.014549	55.85	<2e-16	***
PLS	(Intercept)	0.089182	0.008385	10.64	<2e-16	***
	y	0.818459	0.014357	57.01	<2e-16	***
DNN	(Intercept)	0.061944	0.007447	8.318	4.63e-16	***
	y	0.965925	0.012751	75.756	< 2e-16	***
Sig Code	0 '***'	0.001 '**'	0.01 '*	0.05 '.'		

Table 6. Linear fit statistics for chemometric models as reported by R. Both slope and intercepts of all models were found to be significant.

ness using the statistical analysis software package, R. Based on the results of the analysis of residuals, it was expected that some other factor will show as significant. One-way analysis of variance (ANOVA) was performed to evaluate the independence of nuisance factors from the resultant data. Specifically, it was performed to determine whether or not the date of sample mixture, the order of samples tested and

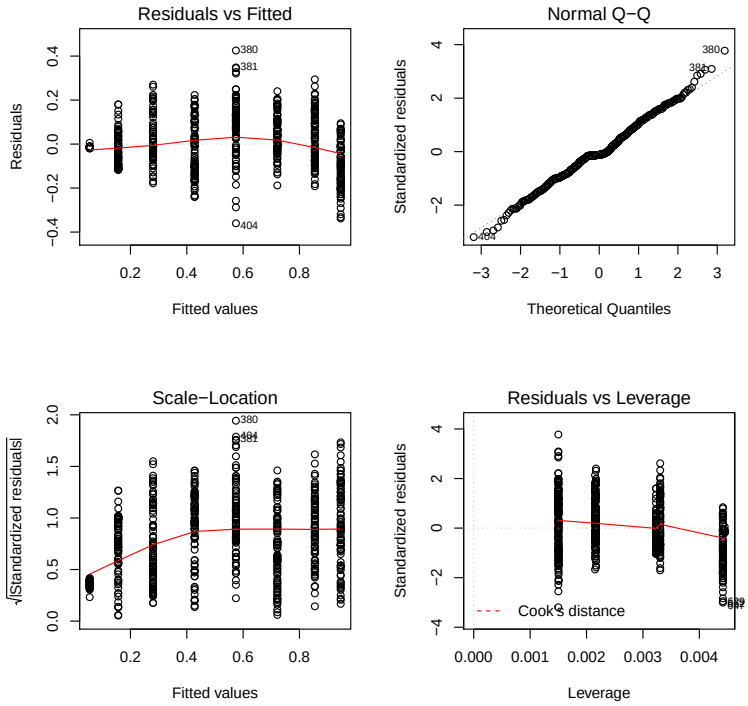

Figure 31. Residual plots for DNN results performed on experimental data. The Normal QQ plot shows a nearly normal distribution of residuals. The residuals vs fitted plot shows a pattern of residual distribution with ^{6}Li fraction, and the Scale-Location plot shows that the variance of data changes slightly as well. Residuals vs Leverage shows that no outliers remain that should significantly affect the model.

the order of spectra taken within each sample had any impact on the results. If one of these was found to be significant, then it would be indicative of a process related to one of them influencing the data (e.g. samples polluted on one day of mixing, a spectral variation related to the succession of shots, a spectral variation related to the way the data were taken day-to-day).

This was performed by building three linear models. The first, by fitting the model predictions to the known sample ^{6}Li fraction. A second, third and fourth, by including the date of sample mixture (mix date), date of sample collection (shot date) and the order of spectra taken within each concentration sample data (inner order), respectively. Each of the third, fourth and fifth models were then compared by ANOVA to the first model results.

The very high significance in the second and third models in PCA and PLS, and the same in the second model in DNN, and very low significance in the concentration for all, shows that the included nuisance factor has an effect on the prediction (see table 7). Taken together with the best performance by the DNN, it is believed

Model / Nuisance	Res.Df	RSS	Df	Sum of Sq	F	Pr(>F)	Sig
PCA	702	10.1615					
Mix Date	700	9.2513	2	0.91022	34.436	5.438e-15	***
Shot Date	701	9.8537	1	0.30782	21.898	3.451e-06	***
Inner Order	603	9.2541	99	0.90737	0.5972	0.9991	
PLS	702	10.1615					
Mix Date	700	9.2513	2	0.91022	34.436	5.438e-15	***
Shot Date	701	9.8537	1	0.30782	21.898	3.451e-06	***
Inner Order	603	9.2541	99	0.90737	0.5972	0.9991	
DNN	702	8.015					
Mix Date	700	8.003	2	0.012051	0.527	0.5906	
Shot Date	701	7.8005	1	0.21451	19.277	1.305e-05	***
Inner Order	603	7.193	99	0.82203	0.6961	0.9869	
Sig Code	0 '***'	0.001 '**'	0.01 '*	0.05 '.'	0.1 ' '	1.0	

Table 7. ANOVA on linear models. Model column indicate factors included in the model, the first as concentrations only, and subsequent models add mixture date shot date and (inner) order. Very high significance in second and third models, and very low significance in concentration, indicate influence by another factor is preferred by the model. Taken with residuals analysis results, this shows model insufficiency.

that this is due to the insufficiency of the model. By adding the nuisance factor, it effectively gives each model a way to correct for non-normality in the residuals (i.e. layering another relationship on top of the predictor-predicted relationship to reduce residuals).

4.2.2.5 Interpretation of ANOVA resuls and removal of 0.95 ^{6}Li fraction sample from model.

Visual inspection of the regression results shows a pronounced bend at the higher concentration end of the model, between the 0.855 and 0.95 ^{6}Li fraction samples. This suggests that the spectra from the 0.95 ^{6}Li fraction sample are predicted to be lower in concentration than they are - a characteristic of self-absorption.

As discussed previously, this well-known phenomena in LIBS plasmas manifests as a reduction in the intensity of a spectral line due to preference of a plasma to absorb

its own emission [28]. Effectively, atoms in the cooler, outer region of the plasma absorbs photons emitted by atoms in the warmer, inner region of the plasma. In this case, we would expect that self-absorption of ^{6}Li emission would show in the model as predictions of less concentration than is actually present.

This result is exactly what is observed in these data. Further, the magnitude of this bend is much less in the DNN results than in the PCA and PLS results. As DNN are capable of modeling non-linear effects, this suggests that the logarithmic self-absorption effect on emission intensity is captured in the DNN results. To remove the impact of this effect on the model, the chemometric analysis process was re-applied to the spectra without the 0.95 ^{6}Li fraction sample in the model.

This application was performed by simply removing the 0.95 ^{6}Li fraction sample data from the analysis set. The new set was again reduced so that there were a balanced number of samples for each concentration. 90 samples were taken from each set of spectra for analysis. The prediction means and errors are provided in table 8.

	PCA Prediction		PLS Prediction		DNN Prediction	
^{6}Li Fraction	$\hat{y} \pm \sigma$	% $(100\times\sigma/\hat{y})$	$\hat{y} \pm \sigma$	% $(100\times\sigma/\hat{y})$	$\hat{y} \pm \sigma$	% $(100\times\sigma/\hat{y})$
0.0300	0.0288±0.0336	116.3617	0.0287±0.0337	117.3355	0.0522±0.0183	35.0815
0.1346	0.1717±0.0709	41.2991	0.1735±0.0691	39.8351	0.1502±0.0768	51.1392
0.2622	0.2989±0.0781	26.1420	0.2995±0.0778	25.9650	0.3134±0.1013	32.3274
0.4145	0.3955±0.0906	22.9095	0.3960±0.0901	22.7392	0.4009±0.0992	24.7331
0.5658	0.5827±0.0620	10.6488	0.5804±0.0645	11.1168	0.5701±0.0639	11.2017
0.7177	0.7118±0.0946	13.2946	0.7112±0.0936	13.1596	0.6582±0.0734	11.1565
0.8551	0.7906±0.1035	13.0908	0.7907±0.1020	12.8999	0.7780±0.1089	13.9959

Table 8. Prediction means and error for chemometric models with 0.95 ^{6}Li fraction sample excluded. Absolute error is now greatest in the DNN. This suggests a reduction in the non-linear pattern of the data found with the 0.95 ^{6}Li fraction sample included.

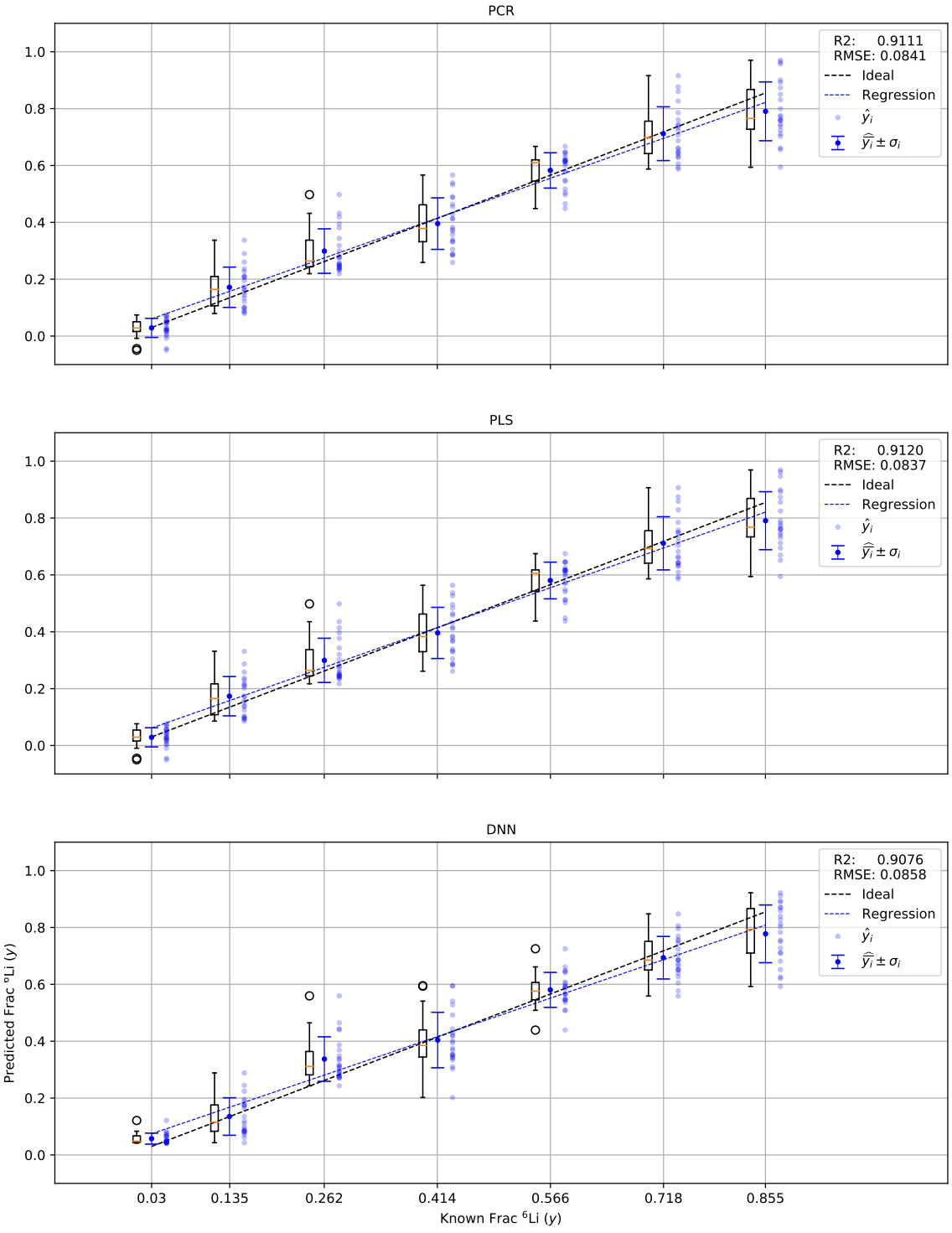

Figure 32. Regression results for PCA, PLS and DNN with the 0.95 ^{6}Li fraction sample excluded. Three representations of the data are presented simultaneously for each method. For each concentration of ^{6}Li, prediction means and standard deviation are represented centered on the concentration value, predictions are shown offset left, box plot with whiskers to 1.5 interquartile ranges offset the right. The DNN now performs worse than does PCA or PLS in both R^2 and RMSE.

With 10 PCs and 7 features used by PCA and PLS, respectively to produce R^2 values of 0.9111 and 0.9120, as well as RMSE values of 0.0841 and 0.0837. Again, 100 runs of the DNN were performed and produced an R^2 of 0.903±0.009 and an RMSE of 0.088±0.004 . It is apparent that the DNN has much more similar performance to the PCA and PLS methods owing to more linearity in the model desired by removal of the 0.95 ^{6}Li fraction sample. Now, all sample data in the test sets are within two standard deviations with the exception of one point in the 0.262 ^{6}Li fraction sample (see figure 32). PCA and PLS weights given in table 9.

w_i	PCA	PLS	w_i	PCA	PLS
w_0	0.0919	0.0000	w_8	0.0347	0.0000
w_1	-0.0135	0.0214	w_9	0.0175	0.4951
w_2	0.0292	-0.0487	w_{10}	-0.1173	-0.7362
w_3	0.0205	0.0786	w_{11}	0.0476	0.3291
w_4	0.0684	0.0290	w_{12}	-0.0036	-0.0163
w_5	0.0661	-0.3439	w_{13}	1.1862	0.0494
w_6	-0.0567	0.5212	w_{14}	0.0000	0.0686
w_7	0.0129	-0.3816	w_{15}	0.0000	-0.0422

Table 9. PLS and PCA regression weights from linear model fitting with 0.95 ^{6}Li fraction sample excluded. All values are shown, not only the values given for the best fit. x_i are the weights given to the corresponding pixel (indexed to zero) in determining the predicted value .

Analysis of residuals in PCA shows the pattern of residual centering nearly removed and much less change in sample variance, if slightly increasing. Residuals appear near normally distributed, and again no outlier appears to influence the residuals in a significant way (see figure 33).

The results are much the same for PLS as the pattern of residual centering is nearly removed but a small increase in sample variance detected. Residuals appear near normally distributed, and again no outlier appears to influence the residuals in a significant way (see figure 34).

The DNN performed least well here, but results are similar to those seen in PCA and PLS. The pattern of residual centering is again nearly removed but a small increase in sample variance detected. Residuals appear near normally distributed,

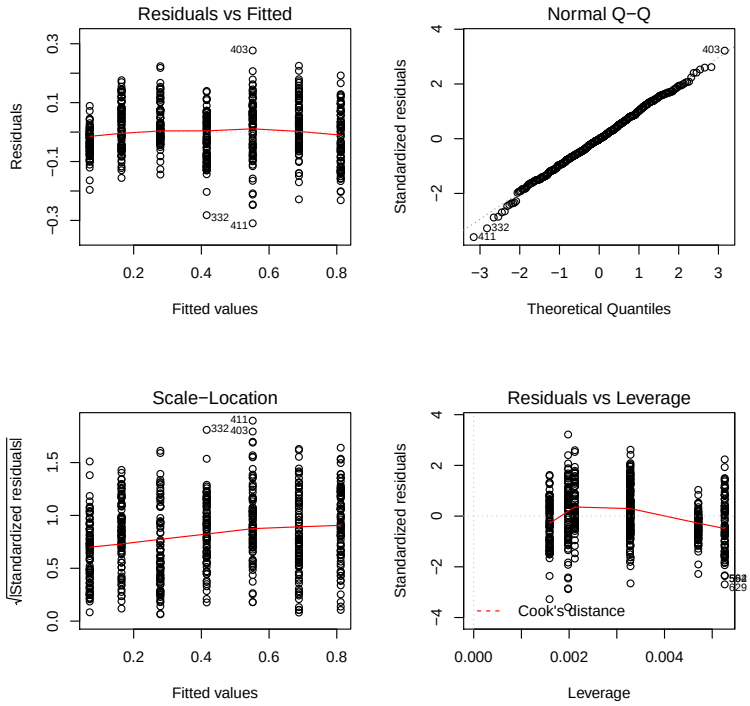

Figure 33. Residual plots for PCA results performed on experimental data with 0.95 ^{6}Li fraction sample excluded. The Normal QQ plot shows a nearly normal distribution of residuals. The residuals vs fitted plot shows a pattern of residual distribution with ^{6}Li fraction, and the Scale-Location plot shows that the variance of data changes slightly as well. Residuals vs Leverage shows that no outliers remain that should significantly affect the model.

and again no outlier appears to influence the residuals in a significant way (see figure 35).

Model coefficients again appeared to be significant with the DNN having, marginally, the least well-defined intercept value (see table 10).

Model	Coefficient	Estimate	Std. Error	t value	Pr(>|t|)	Sig
PCA	(Intercept)	0.043156	0.006215	6.944	9.57e-12	***
	y	0.898628	0.012168	73.849	< 2e-16	***
PLS	(Intercept)	0.043149	0.006197	6.963	8.4e-12	***
	y	0.898644	0.012132	74.072	< 2e-16	***
DNN	(Intercept)	0.025888	0.006638	3.90	0.000106	***
	y	1.036445	0.012995	79.75	< 2e-16	***
Sig Code	0 '***'	0.001 '**'	0.01 '*'	0.05 '.'		

Table 10. Linear fit statistics for chemometric models with 0.95 ^{6}Li fraction sample excluded as reported by R. Both slope and intercepts of all models were found to be significant.

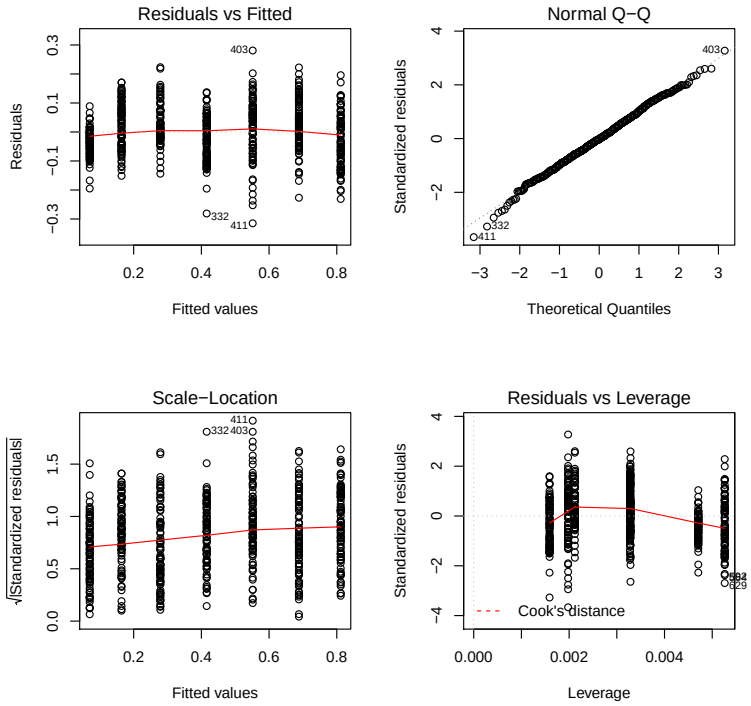

Figure 34. Residual plots for PLS results performed on experimental data with 0.95 ^{6}Li fraction sample excluded. The Normal QQ plot shows a nearly normal distribution of residuals. The residuals vs fitted plot shows a pattern of residual distribution with ^{6}Li fraction, and the Scale-Location plot shows that the variance of data changes slightly as well. Residuals vs Leverage shows that no outliers remain that should significantly affect the model.

ANOVA shows now that the nuisance factors hold very little sway on the model for PCA and PLS. While there is some effect from shot date, which suggests that the experimental set-up or sample response changed between the two days, it is below a 5% probability that this nuisance factor helps to explain predictions. For the DNN, the effect of the mix date was significant and believed, but not proven, to be attributable to the combination of a non-linear model with the three mix dates.

Visual inspection, model fit parameters, analysis of residuals and analysis of variance shows that the model with the 0.95 ^{6}Li fraction sample excluded is superior to the one with the 0.95 ^{6}Li fraction sample included, and supports the supposition that self-absorption affected the sample spectra for the 0.95 ^{6}Li fraction sample.

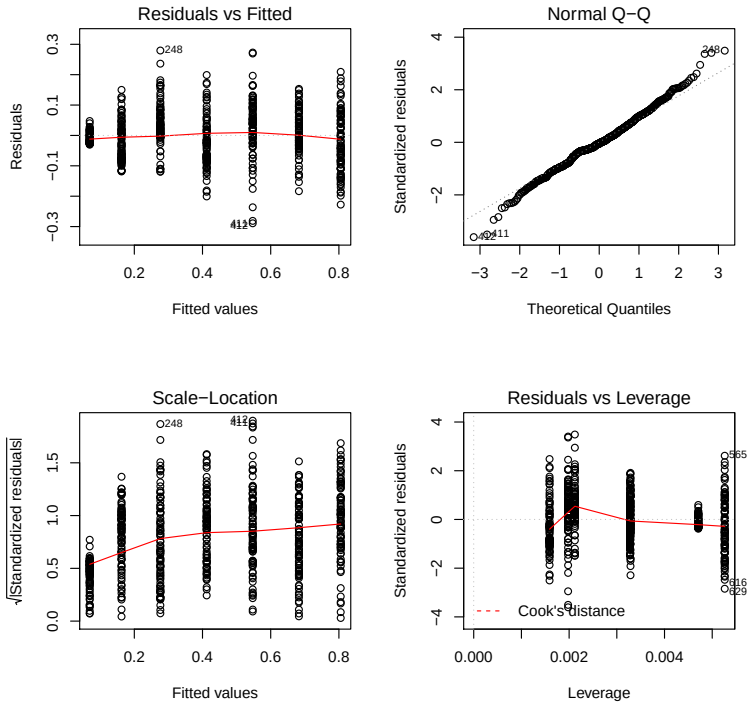

Figure 35. Residual plots for DNN results performed on experimental data with 0.95 ^{6}Li fraction sample excluded. The Normal QQ plot shows a nearly normal distribution of residuals. The residuals vs fitted plot shows a pattern of residual distribution with ^{6}Li fraction, and the Scale-Location plot shows that the variance of data changes slightly as well. Residuals vs Leverage shows that no outliers remain that should significantly affect the model.

Model / Nuisance	Res.Df	RSS	Df	Sum of Sq	F	Pr(>F)	Sig
PCA	628	4.6659					
Mix Date	626	4.6592	2	0.006681	0.4488	0.6386	
Shot Date	627	4.6480	1	0.017939	2.4199	0.1203	
Inner Order	529	4.0576	99	0.60834	0.8011	0.9129	
PLS	628	4.6381					
Mix Date	626	4.6328	2	0.0052468	0.3545	0.7017	
Shot Date	627	4.6173	1	0.020747	2.8172	0.09376	.
Inner Order	529	4.0298	99	0.60825	0.8065	0.9062	
DNN	628	5.3216					
Mix Date	626	5.0770	2	0.24463	15.082	4.009e-07	***
Shot Date	627	5.2989	1	0.022682	2.6838	0.1019	
Inner Order	529	4.6301	99	0.69146	0.798	0.9167	
Sig Code	0 '***'	0.001 '**'	0.01 '*	0.05 '.'	0.1 ' '	1.0	

Table 11. ANOVA on linear models with 0.95 ^{6}Li fraction sample excluded. Model column indicate factors included in the model, the first as concentrations only, and subsequent models add mixture date shot date and (inner) order. Very high significance in only the second model in the DNN indicate influence by the other factors is insignificant, and that the model better fits the data. Taken with residuals analysis results, this shows improved model sufficiency.

4.2.3 Low Resolution LAMIS.

Samples were ablated inside of a low pressure, argon-backfilled chamber with the laser incident, and light collected, at a 45° angle to the sample. The laser pulse was nominally 15 mJ with a 6 ns pulse width, and produced a spot size of approximately 725 μm in diameter when focused through a lens with 130 mm focal length (see figure 21). Spectra of 10-50 on-CCD accumulations were collected using a 350 mm monochromator, and a gate delay varying between 5 μs and 50 μs with gate widths ranging from 10 μs to 1 ms were used with an ICCD gain varied from minimum to maximum intensification (255/255). Previously published results suggest that a LiH molecular bandhead can be found in the 350-400 nm range [45], that of LiO in the 450 and 570 nm range [50]. All attempts failed to observe a molecular shift in transition lines from 300-1100 nm, to include those predicted by the LEVEL simulation near 1000 nm (see figure 36). This is believed to be due to the low intensity of molecular emissions by lithium-bearing molecules in the LPP at the times of observation.

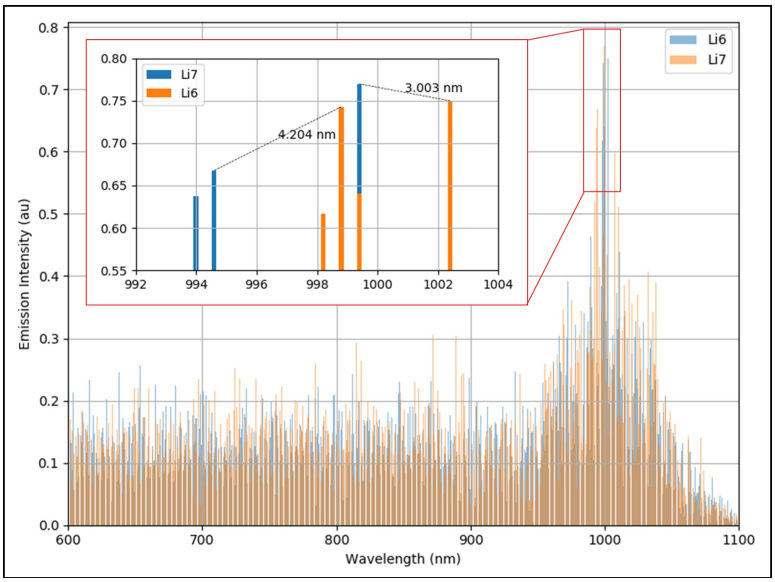

Figure 36. Computer simulation of molecular emissions from the first vibrational state of LiH using LEVEL. LEVEL is a program introduced in 2017 that simulates molecular rotational and vibrational emissions by solving the radial Schrödinger equation for bound and quasibound levels [38].

V. Findings and Conclusions

In this research, three chemometric analysis techniques were applied to spectra collected by LIBS to determine their ability to quantitatively determine the concentrations of lithium isotopes in solid, prepared samples of $LiOH{\cdot}H_2O$. Spectra were collected by LIBS using the lithium atomic emission lines near 670.7 nm. The same was attempted with LAMIS using the molecular lines of LiH and LiO expected in the region of 350-570 nm, but these lines were not observed.

5.1 Findings.

LIBS, using chemometrics, was found to provide an accurate if imprecise method for quantitatively determine concentrations of lithium isotopes. This technique used a 1,500 mW Nd:YAG laser and a 750 mm spectrometer achieving 70 pm resolution. Sample ablation occurred in an argon purged, low pressure vacuum chamber. Spectra consisting of the summation of 20 accumulations were collected from 1-2 μs after ablation. This technique could be improved by the use of a higher resolution spectrometer, or a double-pulse laser set up.

To the author's knowledge, self-absorption of isotopic emission in a LPP was observed experimentally in this work for the first time. In medium resolution LIBS experiments, reduced intensity in the 0.95 ^{6}Li atom fraction sample is attributed to self-absorption, which can be prevalent in LIBS plasmas with high concentrations of analyte [28]. Self-absorption can occur in resonance lines where the lower energy level of the transition is the ground state of the atom [28], of which the observed lines are. This matrix effect usually results in flat topped peaks or inverted peaks as the atoms within the plasma, generally concentrated on the periphery where temperatures are lower and more atoms of a lower energy state would be expected, and which would

absorb the light emitted from the central, hottest part of the plasma [28]. Little evidence of peak cropping, or inversion, is observed as the emission lines that make up the analyzed spectra are unresolved between two pixels. The novel nature of this finding was confirmed by an exhaustive literature search.

After adjusting for self-absorption, the difference in data taken were shown to be statistically significant, with PCA and PLS minimum p-values of 0.09376 when including shot date as a model factor. The DNN ANOVA test of mix date showed very high significance, which seems to indicate that the linear model gets better if the mix date data are included in the model. This result is in contrast to the PCA and PLS results, which are interpretable as they produce linear models inherently, and taken to mean ANOVA on DNN results are inaccurate. Overall, the ANOVA results lend strong support to the accuracy of the data in that experimental error did not significantly alter results.

PCA and PLS demonstrated nearly identical abilities to detect enrichment of $LiOH{\cdot}H_2O$. After adjusting for self-absorption, all methods were able to predict sample concentration with good linearity ($R^2 > 0.90$) and moderate precision (RMSE $<$ 0.09). With RMSE values near 0.084 with only 22 samples used for analysis, both PCA and PLS models can determine small changes in ^{6}Li enrichment, and to detect depletion as the ^{6}Li given sufficient samples.

The NNA created a model with similar capabilities. The lack of success of these models to quantitatively determine the concentrations of ^{6}Li with better accuracy is attributed to the low shot-to-shot variation induced by physical matrix effects, believed to be caused by sample heterogeneity. Figure 26 demonstrates the relative instability of mixed to unmixed samples. If this variation is improved, so too should be the model and prediction accuracy.

The low resolution of the detection system by comparison to the isotopic shift

makes accurate isotopic concentration measurements very difficult without the application of chemometrics. Improving resolution to allow resolving the peaks of ^{6}Li and ^{7}Li should improve prediction accuracy, but can be limited by decreasing signal intensity. Using all three stages of the TriVista 777 reduced the intensity of LPP emission to point that it was noise dominated. Future work will be applied to this problem by implementing DP-LIBS, which has been shown to significantly improve SNR.

If no other adjustments are made, this imprecise technique requires a large sample size for accuracy. By the central limit theorem [68], the 95% confidence interval on the sample mean can be found by

$$\mu_c \pm 1.96\frac{s}{\sqrt{n}} \tag{5}$$

where μ_c is the sample mean, 1.96 is the number of standard deviations needed to include 95% of the normal distribution, s is the standard deviation of predictions and n is the sample size ($s/\sqrt{n}$ is referred to as the standard error the mean, σ_{SEM}). This technique used 100 spectra of 10 accumulations for each sample concentration. 12 of those spectra were removed during outlier rejection, and 66 were used to build the model, so the statistics reported are found from the predictions of the remaining 22 spectra.

If we assume that the sample standard deviation found is a good estimate of the population standard deviation, then to achieve 95% confidence intervals of 0.01 fraction ^{6}Li using PLS, table 12 gives the number of samples required by equation 5. In the most imprecise sample, 3,997 spectra of 10 accumulations would be required. Given a complete calibration model (i.e. no spectra used to build a model) this would take 39,970 laser shots. At a laser repetition rate of 10 hertz repetition rate would take nearly 67 minutes of experiment time.

^{6}Li Fraction	Spectra Required to attain 1% abs. uncertainty	Minutes at 10 Hz
0.0300	438	7.3
0.1346	1836	30.6
0.2622	2324	38.7
0.4145	3116	51.9
0.5658	1600	26.7
0.7177	3366	56.1
0.8551	3997	66.6

Table 12. The number of samples required to reach a 95% confidence interval of 1% for each sample concentration. This suggests that depletion or enrichment could be detected in as little as two minutes.

It is believed that molecular spectra were not observed due to their reduced emission intensity from LPPs in the timescales used (10-100 μs). The lithium hydroxide monohydrate samples used in this research are believed to contain sufficient elemental abundance to form lithium hydride and lithium oxide, but if such were formed in the LPP their population was so small it was not observed.

5.2 Conclusions.

This research quantitatively determined the concentrations of ^{6}Li by using modest LIBS equipment and chemometrics to distinguish spectra unresolved spectral lines differing by isotopic shifts of less than 20 pm. This work demonstrates the ability of chemometric techniques to improve quantitative determination of concentrations of isotopes through analysis of spectra collected via LIBS. Specifically, where no isotopic prediction could have been taken from these data using standard methods, a relatively accurate prediction of isotopic concentration has been demonstrated.

Additionally, it has been statistically postulated that by increasing the sample size, 95% confidence intervals of just 1% absolute uncertainty could be achieved in less than 70 minutes for all sample concentrations up to 0.8551 atom fraction ^{6}Li. This analysis also suggests that depletion of lithium could be detected in less than eight minutes, and enrichment in thirty minutes.

The results of this research have implications for LIBS as a technique to quanti-

tatively determine isotopic concentrations in a field environment, specifically for very light isotopes where other methods fall short. Despite the resolution of the spectrometer used by comparison to the difference of interest, chemometrics was able to achieve the primary goal of this research in this set up using only SP-LIBS. By application of DP-LIBS or even LAMIS to collect spectra, the same road map of analysis could be followed to produce detectors capable of detecting clandestine isotopic enrichment during inspections of nuclear and chemical facilities, and perhaps even in post-blast analysis missions.

5.3 Recommendations for Future Work.

Below are some recommended topics of research identified in the process of completing this work. They are in no particular order.

Validating self-absorption of isotopes of lithium atomic emission lines. The practice used by Bujalic *et. al.* of comparing the emission spectra with and without a spherical mirror behind the LPP [69] could be used for this research. This phenomenon was not found in the literature review of LIBS research for this thesis. While LIBS is not usually used for isotopic measurement, the adoption of chemometrics in this thesis has demonstrated some limited ability to quantitatively determine isotopic concentrations of lithium that may be useful.

Characterizing Stark shift over time. Lithium line stark shifts in LPPs may help to inform the formation of lithium-bearing molecule formation. This could improve our understanding by describing the evolution of electron density and the preference of lithium to recombine in the presence of larger and more easily ionized elements such as oxygen.

Observation of lithium hydride or lithium oxide molecular emissions using DP-LIBS. These lines were not found in this research, and other LAMIS work has not

been performed on lithium isotope measurements. LAMIS seems to provide all of the advantages necessary to allow for field-portable devices capable of lithium isotope measurement. The apparent absence of LiH and LiO lines in the experiments in this thesis could be investigated to better understand the chemistry of lithium molecule formation in LPPs.

Prototyping (in partnership with industry) a field-portable rapid isotopic detection system. This is the natural progression of the effort to develop these devices, and several companies seem poised to develop them. The capability to perform this measurement in lithium should also provide a capability to measure other light isotopes in the field, which could augment the limitations of portable x-ray fluorescence devices. This would include determining minimum requirements for lithium detection to be performed using LAMIS.

Bibliography

1. M. Dayah, "Ptable: The Interactive Periodic Table," Online, 1997. [Online]. Available: https://ptable.com

2. I. News, "Lithium Reserves by Country," Online, 2019, accessed: 29 September 2019. [Online]. Available: https://investingnews.com/daily/resource-investing/battery-metals-investing/lithium-investing/lithium-reserves-country/

3. T. A. Archive, "The Hydrogen Bomb: The Basics," Online, 1998-2015, accessed: 29 September 2019. [Online]. Available: https://www.atomicarchive.com/Fusion/Fusion2.shtml

4. The Smithsonian National Air and Space Museum, "Lithium Hydroxide Canister, Mock-Up, Apollo 13 Emergency," Online, accessed: 29 September 2019. [Online]. Available: https://airandspace.si.edu/collection-objects/lithium-hydroxide-canister-mock-apollo-13-emergency

5. T. Giegerich, C. Day, R. Knitter, and N. Osman, "Lithium enrichment issues in the sustainable supply chain of future fusion reactors," Institute for Technical Physics, Karlsruhe Institue of Technology, 2016. [Online]. Available: https://nucleus.iaea.org/sites/fusionportal/Technical%20Meeting%20Proceedings/1st%20IAEA%20TM%20on%20Fusion%20Power%20Plant%20Safety/Presentations/Giegerich.pdf

6. M.B. Chadwick, P. Obložinský, M. Herman, N.M. Greene, R.D. McKnight, D.L. Smith, P.G. Young, R.E. MacFarlane, G.M. Hale, S.C. Frankle, A.C. Kahler, T. Kawano, R.C. Little, D.G. Madland, P. Moller, R.D. Mosteller, P.R. Page, P. Talou, H. Trellue, M.C. White, W.B. Wilson, R. Arcilla, C.L. Dunford, S.F. Mughabghab, B. Pritychenko, D. Rochman, A.A. Sonzogni, C.R. Lubitz, T.H. Trumbull, J.P. Weinman, D.A. Brown, D.E. Cullen, D.P. Heinrichs, D.P. McNabb, H. Derrien, M.E. Dunn, N.M. Larson, L.C. Leal, A.D. Carlson, R.C. Block, J.B. Briggs, E.T. Cheng, H.C. Huria, M.L. Zerkle, K.S. Kozier, A. Courcelle, V. Pronyaev, S.C. van der Marck, "ENDF/B-VII.0: Next generation evaluated nuclear data library for nuclear science and technology," 2019.

7. D. Cremers, A. Beddingfield, R. Smithwick, R. C. Chinni, C. R. Jones, B. Beardsley, and L. Karch, "Monitoring Uranium, Hydrogen, and Lithium and Their Isotopes Using a Compact Laser-Induced Breakdown Spectroscopy (LIBS) Probe and High-Resolution Spectrometer," *Applied Spectroscopy*, vol. 66, no. 3, pp. 250–261, 2012.

8. BRGM, "Lithium isotopes: an innovative tool for the geosciences," online, 2015. [Online]. Available: https://www.brgm.eu/project/lithium-isotopes-innovative-tool-geosciences

9. C. A. Smith and M. A. Martinez, "Laser induced breakdown spectroscopy (libs) applied to plutonium analysis," *AIP Conference Proceedings*, vol. 532, no. 1, pp. 305–306, 2000. [Online]. Available: https://aip.scitation.org/doi/abs/10.1063/1.1292305

10. C. A. Smith, M. A. Martinez, D. Veirs, and D. A. Cremers, "Pu-239/pu-240 isotope ratios determined using high resolution emission spectroscopy in a laser-induced plasma," *Spectrochimica Acta Part B: Atomic Spectroscopy*, vol. 57, no. 5, pp. 929 – 937, 2002. [Online]. Available: http://www.sciencedirect.com/science/article/pii/S058485470200023X

11. M. Miyabe, M. Oba, K. Jung, H. Iimura, K. Akaoka, M. Kato, H. Otobe, A. Khumaeni, and I. Wakaida, "Laser ablation absorption spectroscopy for isotopic analysis of plutonium: Spectroscopic properties and analytical performance," *Spectrochimica Acta Part B: Atomic Spectroscopy*, vol. 134, pp. 42 – 51, 2017. [Online]. Available: http://www.sciencedirect.com/science/article/pii/S0584854717301416

12. D. W. T. Griffith, I. Jamie, M. Esler, S. R. Wilson, S. D. Parkes, C. Waring, and G. W. Bryant, "Real-time field measurements of stable isotopes in water and co2 by fourier transform infrared spectrometry," *Isotopes in Environmental and Health Studies*, vol. 42, no. 1, pp. 9–20, 2006, pMID: 16500751.

13. J. R. Köster, R. Well, B. Tuzson, R. Bol, K. Dittert, A. Giesemann, L. Emmenegger, A. Manninen, L. Cárdenas, and J. Mohn, "Novel laser spectroscopic technique for continuous analysis of n2o isotopomers – application and intercomparison with isotope ratio mass spectrometry," *Rapid Communications in Mass Spectrometry*, vol. 27, no. 1, pp. 216–222, 2013.

14. "Nuclear posture review report," Internet, 2018.

15. "Report: North korea's lithium 6 production for nuclear weapons," online, 2017.

16. J. E. Barefield, E. J. Judge, J. M. Berg, S. P. Willson, L. A. Le, and L. N. Lopez, "Analysis and spectral assignments of mixed actinide oxide samples using laser-induced breakdown spectroscopy (libs)," *Applied Spectroscopy*, vol. 67, pp. 433–440, 2013.

17. M. Z. Martin, S. Allman, D. J. Brice, R. C. Martin, and N. O. Andre, "Exploring laser-induced breakdown spectroscopy for nuclear materials analysis and in-situ applications," *Spectrochimica Acta Part B: Atomic Spectroscopy*, vol. 74-75, pp. 177 – 183, 2012, 6th Euro-Mediterranean Symposium on Laser Induced Breakdown Spectroscopy (EMSLIBS 2011). [Online]. Available: http://www.sciencedirect.com/science/article/pii/S0584854712001814

18. M. B. Shattan, D. J. Miller, M. T. Cook, A. C. Stowe, J. D. Auxier, C. Parigger, and H. L. Hall, "Detection of uranyl fluoride and sand surface contamination

on metal substrates by hand-held laser-induced breakdown spectroscopy," *Appl. Opt.*, vol. 56, no. 36, pp. 9868–9875, Dec 2017.

19. "Chemometrics: Understanding Chemical Data," accessed 29 September 2019. [Online]. Available: https://www.camo.com/chemometrics/

20. X. Xu, "Fast and Simultaneous Determination of Soil Properties Using Laser-Induced Breakdown Spectroscopy (LIBS): A Case Study of Typical Farmland Soils in China," *Soil Systems*, vol. 3, no. 4, p. 66, 2019.

21. J.-B. Sirven, B. Bousquet, L. Canioni, L. Sarger, S. Tellier, M. Potin-Gautier, and I. Le Hécho, "Qualitative and quantitative investigation of chromium-polluted soils by laser-induced breakdown spectroscopy combined with neural networks analysis," *Analytical and bioanalytical chemistry*, vol. 385, pp. 256–62, 06 2006.

22. N. Konjević, A. Lesage, J. R. Fuhr, and W. L. Wiese, "Experimental Stark Widths and Shifts for Spectral Lines of Neutral and Ionized Atoms (A Critical Review of Selected Data for the Period 1989 Through 2000)," *Journal of Physical and Chemical Reference Data*, vol. 31, no. 3, pp. 819–927, 2002.

23. V. Rai, F.-Y. Yueh, and J. Singh, "Theoretical model for double pulse laser-induced breakdown spectroscopy," *Applied optics*, vol. 47, pp. G30–G37, 12 2008.

24. J. Hermann, L. Mercadier, E. Axente, and S. Noël, "Properties of plasmas produced by short double pulse laser ablation of metals," *Journal of Physics: Conference Series*, vol. 399, p. 012006, nov 2012. [Online]. Available: https://doi.org/10.1088%2F1742-6596%2F399%2F1%2F012006

25. D. Hahn and N. Omenetto, "Laser-induced breakdown spectroscopy (libs), part ii: Review of instrumental and methodological approaches to material analysis and applications to different fields," *Applied spectroscopy*, vol. 66, pp. 347–419, 04 2012.

26. G. Rieger, M. Taschuk, Y. Tsui, and R. Fedosejevs, "Comparative study of laser-induced plasma emission from microjoule picosecond and nanosecond krf-laser pulses," *Spectrochimica Acta Part B: Atomic Spectroscopy*, vol. 58, no. 3, pp. 497 – 510, 2003. [Online]. Available: http://www.sciencedirect.com/science/article/pii/S0584854703000144

27. S. Zhang, Z. Wang, M. He, Y. Jiang, B. Zhang, W. Hang, and B. Huang, "Laser-induced plasma temperature," *Spectrochimica Acta Part B*, vol. 97, pp. 13–33, 2014.

28. D. Cremers and L. Radziemski, *Handbook of Laser-Induced Breakdown Spectroscopy, 2nd ed.* West Sussex, UK: John Wiley & Sons, 2013.

29. D. Menut, P. Fichet, J.-L. Lacour, A. Rivoallan, and P. Mauchien, "Micro-laser-induced breakdown spectroscopy technique: a powerfulmethod for performing quantitative surface mapping on conductive andnonconductive samples," *Appl. Opt.*, vol. 42, no. 30, pp. 6063–6071, Oct 2003. [Online]. Available: http://ao.osa.org/abstract.cfm?URI=ao-42-30-6063

30. H. Balzer, M. Hoehne, R. Noll, and V. Sturm, "New approach to online monitoring of the al depth profile of the hot-dip galvanised sheet steel using libs," *Analytical and Bioanalytical Chemistry*, vol. 385, no. 2, pp. 225–233, May 2006. [Online]. Available: https://doi.org/10.1007/s00216-006-0347-z

31. S. Jantzi, V. Motto-Ros, F. Trichard, Y. Markushin, N. Melikechi, and A. De Giacomo, "Sample Treatment and Preparation for Laser-Induced Breakdown Spectroscopy," *Spectrochimica Acta Part B: Atomic Spectroscopy*, vol. 115, 11 2015.

32. T. Takahashi and B. Thornton, "Quantitative methods for compensation of matrix effects and self-absorption in LIBS signals of solids," *Spectrochimica Acta - Part B Atomic Spectroscopy*, vol. 138, pp. 31–42, 2017.

33. H.-Y. Moon, K. K. Herrera, N. Omenetto, B. W. Smith, and J. Winefordner, "On the usefulness of a duplicating mirror to evaluate self-absorption effects in laser induced breakdown spectroscopy," *Spectrochimica Acta Part B: Atomic Spectroscopy*, vol. 64, no. 7, pp. 702 – 713, 2009.

34. D. Bulajic, M. Corsi, G. Cristoforetti, S. Legnaioli, V. Palleschi, A. Salvetti, and E. Tognoni, "A procedure for correcting self-absorption in calibration free-laser induced breakdown spectroscopy," *Spectrochimica Acta - Part B Atomic Spectroscopy*, vol. 57, no. 2, pp. 339–353, 2002.

35. M. Cvejić, M. Gavrilović, S. Jovićević, and N. Konjević, "Stark broadening of mg i and mg ii spectral lines and debye shielding effect in laser induced plasma," *Spectrochimica Acta Part B: Atomic Spectroscopy*, vol. 85, pp. 20 – 33, 2013.

36. R. E. Russo, A. Bolshakov, X. Mao, C. P. McKay, D. Perry, and O. Sorkhabi, "Laser Ablation Molecular Isotopic Spectrometry," *Spectrochimica Acta Part B: Atomic Spectroscopy*, vol. 66, pp. 99–104, 02 2011.

37. C. M. Western, "PGOPHER, A Program for Simulating Rotational, Vibrational and Electronic Spectra," *Journal of Quantitative Spectroscopy and Radiative Transfer*, vol. 186, pp. 221–242, 2016.

38. R. LeRoy, "LEVEL: A computer program for solving the radial Schrödinger equation for bound and quasibound levels," *Journal of Quantitative Spectroscopy and Radiative Transfer*, vol. 186, pp. 167 – 178, 2017, satellite Remote Sensing and Spectroscopy: Joint ACE-Odin Meeting, October 2015. [Online]. Available: http://www.sciencedirect.com/science/article/pii/S0022407316300978

39. A. Bolshakov, X. Mao, D. Perry, and R. E. Russo, "Laser Ablation Molecular Isotopic Spectrometry for rare isotopes of the light elements," *Spectroscopy*, vol. 29, pp. 30–39, 06 2014.

40. X. Mao, A. A. Bol'Shakov, D. L. Perry, O. Sorkhabi, and R. E. Russo, "Laser Ablation Molecular Isotopic Spectrometry: Parameter influence on boron isotope measurements," *Spectrochimica Acta - Part B Atomic Spectroscopy*, vol. 66, no. 8, pp. 604–609, 2011. [Online]. Available: http://dx.doi.org/10.1016/j.sab.2011.06.007

41. S. Brown, A. Ford, C. C. Akpovo, J. Martinez, and L. Johnson, "Matrix effects in laser ablation molecular isotopic spectrometry," *Spectrochimica Acta - Part B Atomic Spectroscopy*, vol. 101, pp. 204–212, 2014. [Online]. Available: http://dx.doi.org/10.1016/j.sab.2014.09.003

42. S. Brown, A. Ford, C. A. Akpovo, and L. Johnson, "Mid-IR enhanced laser ablation molecular isotopic spectrometry," *Spectrochimica Acta - Part B Atomic Spectroscopy*, vol. 122, no. July, pp. 178–187, 2016. [Online]. Available: http://dx.doi.org/10.1016/j.sab.2016.07.005

43. R. Ahmed and M. Baig, "A comparative study of single and double pulse laser induced breakdown spectroscopy," *Journal of Applied Physics*, vol. 106, p. 033307, 08 2009.

44. P. Bunker, P. Jensen, A. Karpfen, and H. Lischka, "A theoretical calculation of the rotation-vibration energies for lithium hydroxide, lioh," *Journal of Molecular Spectroscopy*, vol. 135, no. 1, pp. 89 – 104, 1989. [Online]. Available: http://www.sciencedirect.com/science/article/pii/0022285289903573

45. H. Skenderovic, T. Ban, and G. Pichler, "LiH Emission Spectrum from the Glow Discharge in a Heat-Pipe Oven," *Journal of Physics D: Applied Physics*, vol. 33, p. 396, 02 2000.

46. M. Weidman, M. Baudelet, S. Palanco, M. Sigman, P. Dagdigian, and M. Richardson, "Nd:YAG-CO2 double-pulse laser induced breakdown spectroscopy of organic films," *Optics express*, vol. 18, pp. 259–66, 01 2010.

47. C. E. Moore, "Atomic Energy Levels as Derived from the Analysis of Optical Spectra – Hydrogen through Vanadium," *National Standard Reference Data Series*, vol. SRDS-NBS 35 Vol. I, 1971, reprint of NBS Circ. 467, Vol. I, 1949.

48. L. J. Radziemski, R. Engleman, and J. W. Brault, "Fourier-transform-spectroscopy measurements in the spectra of neutral lithium, ^{6}I and ^{7}I (Li I)," *Phys. Rev. A*, vol. 52, pp. 4462–4470, Dec 1995. [Online]. Available: https://link.aps.org/doi/10.1103/PhysRevA.52.4462

49. A. Kramida, Y. Ralchenko, J. Reader, and N. A. Team, NIST Atomic Spectra Database (ver. 5.7.1), [Online]. Available: `https://physics.nist.gov/asd` [2019, December 3]. National Institute of Standards and Technology, Gaithersburg, MD., 2019.

50. J. Woodward, J. Hayden, and J. Gole, "Formation and characterization of a low-lying electronic state of the alkali monoxides lio. . . cso in the red and near infrared," *Chemical Physics*, vol. 134, no. 2, pp. 395 – 419, 1989. [Online]. Available: http://www.sciencedirect.com/science/article/pii/030101048987171X

51. A. Biancolillo and F. Marini, "Chemometric Methods for Spectroscopy-Based Pharmaceutical Analysis," Online, University of Rome La Sapienza, Rome, Italy, accessed 1 October 2019. [Online]. Available: https://www.frontiersin.org/articles/10.3389/fchem.2018.00576/full

52. R. Bro and A. K. Smilde, "Principal Component Analysis," *Analytical Methods*, vol. 6, no. 9, pp. 2812–2831, 2014.

53. V. K. Unnikrishnan, K. S. Choudhari, S. D. Kulkarni, R. Nayak, V. B. Kartha, and C. Santhosh, "Analytical predictive capabilities of laser induced breakdown spectroscopy (libs) with principal component analysis (pca) for plastic classification," *RSC Adv.*, vol. 3, pp. 25 872–25 880, 2013. [Online]. Available: http://dx.doi.org/10.1039/C3RA44946G

54. A. Erdem, A. Çilingiroğlu, A. Giakoumaki, M. Castanys, E. Kartsonaki, C. Fotakis, and D. Anglos, "Characterization of iron age pottery from eastern turkey by laser- induced breakdown spectroscopy (libs)," *Journal of Archaeological Science*, vol. 35, no. 9, pp. 2486 – 2494, 2008. [Online]. Available: http://www.sciencedirect.com/science/article/pii/S0305440308000642

55. Şükriye Nihan Karuk Elmas, F. N. Arslan, G. Akin, A. Kenar, H.-G. Janssen, and I. Yilmaz, "Synchronous fluorescence spectroscopy combined with chemometrics for rapid assessment of cold–pressed grape seed oil adulteration: Qualitative and quantitative study," *Talanta*, vol. 196, pp. 22 – 31, 2019. [Online]. Available: http://www.sciencedirect.com/science/article/pii/S0039914018312931

56. M. Z. Martin, N. Labbé, N. André, S. D. Wullschleger, R. D. Harris, and M. H. Ebinger, "Novel Multivariate Analysis for Soil Carbon Measurements Using Laser-Induced Breakdown Spectroscopy," *Soil Science Society of America Journal*, vol. 74, pp. 87–93, 2010. [Online]. Available: http://dx.doi.org/10.2136/sssaj2009.0102

57. B. G. Oztoprak, J. Gonzalez, J. Yoo, T. Gulecen, N. Mutlu, R. E. Russo, O. Gundogdu, and A. Demir, "Analysis and classification of heterogeneous kidney stones using laser-induced breakdown spectroscopy (libs)," *Applied Spectroscopy*, vol. 66, no. 11, pp. 1353–1361, 2012.

58. Z. Li, X. Zhang, G. A. Mohua, and V. Karanassios, "Correction Using a Large-Size Spectrometer and ANN-Based Deep Learning for a Miniature One," *Intechopen.com*, 2017.

59. X. Mao, G. C. Chan, V. Zorba, and R. E. Russo, "Reduction of spectral interferences and noise effects in laser ablation molecular isotopic spectrometry with partial least square regression - A computer simulation study," *Spectrochimica Acta - Part B Atomic Spectroscopy*, vol. 122, pp. 75–84, 2016.

60. Josh, "Everything You Need to Know About Artificial Neural Networks," Online, 2015, accessed 1 October 2015. [Online]. Available: https://medium.com/technology-invention-and-more/everything-you-need-to-know-about-artificial-neural-networks-57fac18245a1

61. J. Wang, X. Liao, P. Zheng, S. Xue, and R. Peng, "Classification of chinese herbal medicine by laser-induced breakdown spectroscopy with principal component analysis and artificial neural network," *Analytical Letters*, vol. 51, no. 4, pp. 575–586, 2018. [Online]. Available: https://doi.org/10.1080/00032719.2017.1340949

62. E. C. Ferreira, D. M. Milori, E. J. Ferreira, R. M. D. Silva, and L. Martin-Neto, "Artificial neural network for cu quantitative determination in soil using a portable laser induced breakdown spectroscopy system," *Spectrochimica Acta Part B: Atomic Spectroscopy*, vol. 63, no. 10, pp. 1216 – 1220, 2008, a collection of papers presented at the Euro Mediterranean Symposium on Laser Induced Breakdown Spectroscopy (EMSLIBS 2007). [Online]. Available: http://www.sciencedirect.com/science/article/pii/S0584854708002565

63. F.-Y. Yueh, H. Zheng, J. P. Singh, and S. Burgess, "Preliminary evaluation of laser-induced breakdown spectroscopy for tissue classification," *Spectrochimica Acta Part B: Atomic Spectroscopy*, vol. 64, no. 10, pp. 1059 – 1067, 2009, a Collection of Papers Presented at the Fifth International Conference on Laser Induced Breakdown Spectroscopy (LIBS 2008). [Online]. Available: http://www.sciencedirect.com/science/article/pii/S0584854709002237

64. P. J. Rousseeuw, "Least median of squares regression," *Journal of the American Statistical Association*, vol. 79, no. 388, pp. 871–880, 1984.

65. J. Hardin and D. M. Rocke, "Outlier detection in the multiple cluster setting using the minimum covariance determinant estimator," *Computational Statistics and Data Analysis*, vol. 44, no. 4, pp. 625 – 638, 2004.

66. "Conversation with greg smith, air force institute of technology lab supervisor," November 2019.

67. R. D. Cook, "Detection of influential observation in linear regression," *Technometrics*, vol. 19, no. 1, pp. 15–18, 1977.

68. M. Barde and P. Barde, "What to use to express the variability of data: Standard deviation or standard error of mean?" *Perspectives in Clinical Research*, vol. 3, no. 3, pp. 113–116, 2012. [Online]. Available: http://www.picronline.org/article.asp?issn=2229-3485;year=2012;volume=3;issue=3;spage=113;epage=116;aulast=Barde;t=6

69. D. Bulajic, M. Corsi, G. Cristoforetti, S. Legnaioli, V. Palleschi, A. Salvetti, and E. Tognoni, "A procedure for correcting self-absorption in calibration free-laser induced breakdown spectroscopy," *Spectrochimica Acta - Part B Atomic Spectroscopy*, vol. 57, no. 2, pp. 339–353, 2002.

REPORT DOCUMENTATION PAGE

Form Approved
OMB No. 0704–0188

1. REPORT DATE *(DD–MM–YYYY)*	2. REPORT TYPE	3. DATES COVERED *(From — To)*
01–07–2020	Master's Thesis	APR 2019 — MAR 2020

4. TITLE AND SUBTITLE

DETERMINING LITHIUM ISOTOPE CONCENTRATION IN LITHIUM HYDROXIDE MONOHYDRATE USING DOUBLE-PULSE LASER-INDUCED BREAKDOWN SPECTROSCOPY

5a. CONTRACT NUMBER

xxxxxxxxxxxxxxxxxxxx

5b. GRANT NUMBER

5c. PROGRAM ELEMENT NUMBER

6. AUTHOR(S)

LTC Jason Wood, U.S. Army

5d. PROJECT NUMBER

20ENP

5e. TASK NUMBER

5f. WORK UNIT NUMBER

7. PERFORMING ORGANIZATION NAME(S) AND ADDRESS(ES)

Air Force Institute of Technology
Graduate School of Engineering and Management (AFIT/ENP)
2950 Hobson Way
WPAFB OH 45433-7765

8. PERFORMING ORGANIZATION REPORT NUMBER

xxxxxxxxxxxxxxxxxxxx

9. SPONSORING / MONITORING AGENCY NAME(S) AND ADDRESS(ES)

Air Force Technical Applications Center
2950 Hobson Way
WPAFB, OH 45433-7765
DSN 000-000-0000, COMM 000-000-0000
Email: shattan@afit.edu

10. SPONSOR/MONITOR'S ACRONYM(S)

LIBS, SP-LIBS, DP-LIBS

11. SPONSOR/MONITOR'S REPORT NUMBER(S)

12. DISTRIBUTION / AVAILABILITY STATEMENT

DISTRIBUTION STATEMENT A:
APPROVED FOR PUBLIC RELEASE; DISTRIBUTION UNLIMITED.

13. SUPPLEMENTARY NOTES

14. ABSTRACT

15. SUBJECT TERMS

Laser-Induced Breakdown Spectroscopy, Lithium Hydroxide Monohydrate, Isotopic Determination

16. SECURITY CLASSIFICATION OF:			17. LIMITATION OF ABSTRACT	18. NUMBER OF PAGES	19a. NAME OF RESPONSIBLE PERSON
a. REPORT	b. ABSTRACT	c. THIS PAGE			Lieutenant Colonel M. Shattan, AFIT/ENP
U	U	U	U	XXX	19b. TELEPHONE NUMBER *(include area code)* (937) 255-3636, x4555; amy.magnus@afit.edu